Biogeosciences, 23, 8233–8258, 2026
https://doi.org/10.5194/bg-23-8233-2026
© Author(s) 2026. This work is distributed under
the Creative Commons Attribution 4.0 License.

Biogeosciences Open Access EGU

Future projections of compound events around the Main Hawaiian Islands

Tobias Friedrich, Lucia Hošeková, and Brian S. Powell

Department of Oceanography, University of Hawai'i at Mānoa, Honolulu, HI 96822, USA

Correspondence: Tobias Friedrich (tobiasf@hawaii.edu)

Received: 20 March 2026 – Discussion started: 7 April 2026
Revised: 21 September 2026 – Accepted: 21 October 2026 – Published: 12 November 2026

Abstract. The consequences of overlapping environmental stressors – referred to as compound events – may be more harmful to marine ecosystems than as individual stressors. Using recently conducted submesoscale-permitting future projections for the Main Hawaiian Islands, we present the first assessment of future compound events for Hawaiian waters. Our analysis focuses on surface and sub-surface heat-stress, ocean acidification, and low-oxygen events and is based on three different greenhouse gas emission scenarios. We show that a large fraction of ocean around Hawai'i will be subject to compound events in the near future. However, the projected event characteristics such as duration and intensity vary substantially across the region suggesting that potential ecosystem impacts may differ over short distances. Our results reveal that these spatial differences are mainly driven by considerably different magnitudes of natural variability in ocean physics and chemistry across the domain driven by mesoscale processes, while anthropogenic trends exhibit only minor spatial differences. Our analysis demonstrates that small-scale tidal variability can significantly mitigate compound events in near-shore regions, including some designated Marine Protected Areas. Overall, our findings highlight the need for high-resolution numerical models as well as for an extended observation network for robust future projections of local extreme events.

1 Introduction

As a result of human-induced carbon dioxide (CO_2) emissions the oceans have been warming, acidifying, and losing oxygen (IPCC, 2023; Kwiatkowski et al., 2020). All three processes individually can pose a threat to marine organisms and ecosystems as a whole (IPCC, 2023).

Extreme events are typically regarded as infrequent environmental conditions that are outside of the range an organism or ecosystem has adapted to (e.g., marine heat waves or abnormally high acidity or low oxygen concentrations). This range can be defined by absolute thresholds such as the saturation level with respect to aragonite (e.g. Hauri et al., 2016) or by relative thresholds. Relative thresholds are based on the local natural-variability envelope and the assumption that an organism's and/or ecosystem's well-being will be harmed when experiencing conditions outside this amplitude of variability (Burger et al., 2022; Hauri et al., 2024; Wong et al., 2024).

Compound events (CEs) are multiple individual extreme events that overlap in space and time (Gruber et al., 2021). They are believed to be more challenging and harmful than individual extreme events since multiple stressors affect an organism and/or ecosystem at the same time. Numerous studies have been carried out to investigate compound event characteristics (CECs) for the global ocean (Burger et al., 2022; Wong et al., 2024; Mogen et al., 2024) or individual regions such as the Gulf of Alaska (Hauri et al., 2024) or the Equatorial and South Atlantic (Rodrigues et al., 2025). The aim of the present paper is to complement previous studies and to provide detailed regional 21st century projections of CECs for the Main Hawaiian Islands with a focus on high temperature (T), high acidity as represented by hydrogen ion concentration ($[H^+]$), and low oxygen concentration ($[O_2]$).

The Main Hawaiian Islands (MHI, Fig. 1) are located in the oligotrophic southern part of the North Pacific Subtropical Gyre. The marine ecosystem around Hawai'i is home to a rich diversity of marine life including numerous threatened

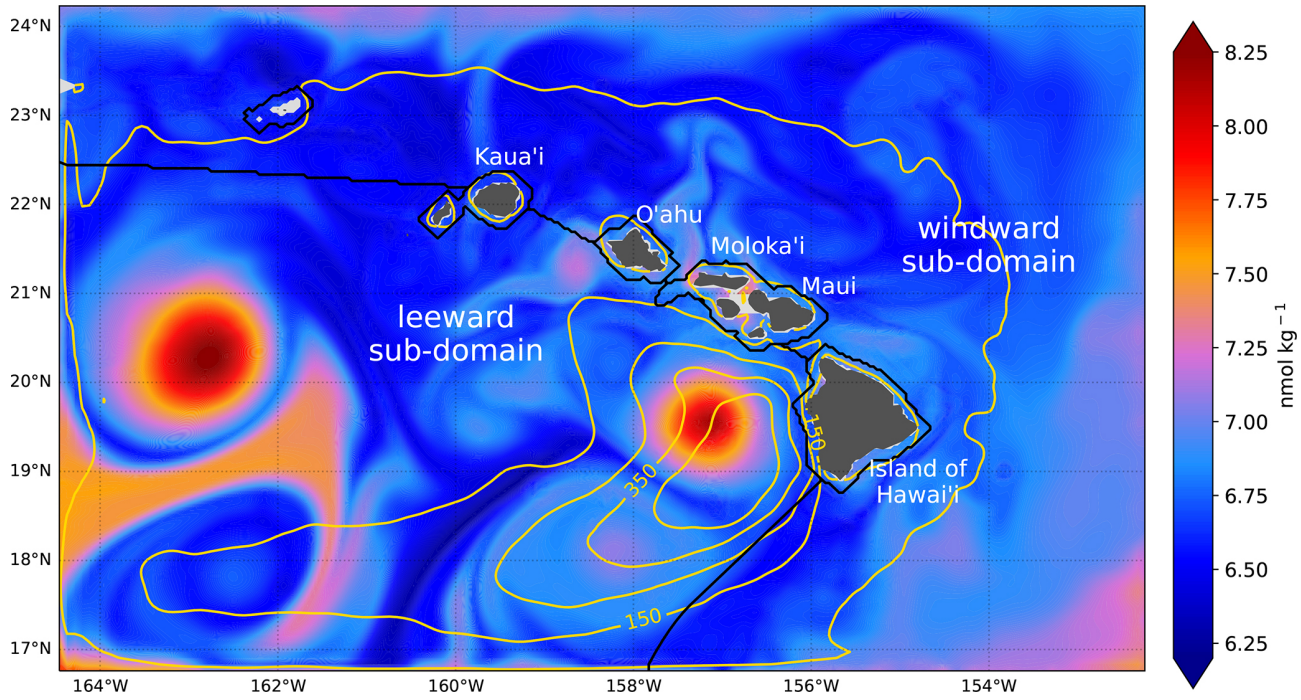


Figure 1. Model domain of the Main Hawaiian Islands. Black lines indicate windward, leeward, and near-shore sub-domains. Shading shows snapshot of hydrogen ion concentration ($[H^+]$) at 100 m water depth (nmol kg^{-1}). Yellow contours depict mean eddy kinetic energy (0–100 m, $cm^2\,s^{-2}$).

and endangered species and the ecosystem is vital to commercial and recreational fishing, culture, health, well-being, and economic stability. The islands are surrounded by coral reefs that provide extensive ecosystem services in the form of livelihoods from fishing and tourism, coastal protection, sustenance, and cultural values.

The waters around the Hawaiian Islands form a dynamically diverse region and are subject to substantial mesoscale and sub-mesoscale variability of physical, biological, and chemical ocean conditions that has to be taken into account when putting anthropogenic trends into the context of natural variability. The archipelago disrupts the north-east trade winds and the North Equatorial Current, generating zones of wind- and current-shear (Chavanne et al., 2002; Xie et al., 2001). The wind-shear pattern can be traced for $\sim$3000 km into the Western Pacific (Xie et al., 2001). The wind- and current-shear give rise to cyclonic and anticyclonic eddies mainly to the west of the islands (Calil et al., 2008; Yoshida et al., 2010; Jia et al., 2011; Azevedo Correia de Souza et al., 2015). Mesoscale eddies can uplift and suppress isopycnals in their center and spin up vertical circulation cells at their fronts. This motion can act on the strong vertical gradients of physical and biogeochemical properties (Barone et al., 2019, 2022; Friedrich et al., 2021) resulting in substantial natural variability in surface and sub-surface areas of high eddy activity. This effect is illustrated by Fig. 1 showing an illustrative snapshot of simulated daily mean hydrogen ion concentration ($[H^+]$) at a water depth of 100 m. It can be seen that the doming of isopycnals in a cyclonic eddy to the west of the Island of Hawai'i and further west in the domain results in strongly increased $[H^+]$ near the center. In contrast, the center of the nearby anti-cyclonic eddy is characterized by decreased $[H^+]$ resulting in a large spatial (and temporal) variability of $[H^+]$ (and related carbonate chemistry variables). It should be noted that this variability is amplified by the fact that the frontal areas between the two eddies are subject to $[H^+]$ anomalies of opposite sign to their respective centers.

In addition to eddy generation, Hawai'i is one of the largest sites in the world for tidal conversion. The tall ocean ridges obstruct the propagation of the barotropic tides (Merrifield and Holloway, 2002; Rainville et al., 2010), converting some of this energy into internal tides within the ocean. This process can lead to vertical displacement of isopycnals and mixing that can generate strong natural variability of physical and biogeochemical properties on semi-diurnal and diurnal timescales.

Results from recent downscaling simulations for the MHI (Friedrich et al., 2024) show that domain-averaged Sea Surface Temperature is projected to increase by 1.64–3.25 °C depending on the greenhouse gas scenario, while pH is projected to drop by 0.08–0.33. Furthermore, near-surface, coastal ocean acidification around Hawai'i is projected to create conditions far outside the natural-variability enve-

lope (Hošeková et al., 2025). Building upon these individual changes, this paper aims to identify how CECs will evolve, vary, and impact the MHI over three climate scenarios.

Our paper is organized as follows: Sect. 2 briefly presents the model and the regional downscaling effort. This section also outlines our definition of CEs and explains the calculation of their characteristics. Section 3 presents projected human-induced trends for the variables of interest and discusses the spatial patterns of their natural variability. Furthermore, Sect. 3 provides an in-depth assessment of CECs projected for different greenhouse gas scenarios, depth bins, as well as their spatial distribution within our domain. Section 3 also discusses potential ecosystem impacts of the projected CECs. The final section summarizes our results.

2 Materials and methods

2.1 Downscaling simulations

Our analysis of future compound events is based on the submesoscale-permitting physical/biogeochemical model projections for the MHI (Fig. 1) presented in Friedrich et al. (2024). We use a total of five downscaling simulations of the 21st century to account for different Shared Socioeconomic Pathways (SSP) scenarios as well as interannual and decadal variability. The foundation for the regional modeling efforts is provided by a submesoscale-permitting physical/biogeochemical model of the MHI presented in Friedrich et al. (2021). To simulate the evolution of ocean physics and biogeochemistry, we use the Regional Ocean Modeling System (ROMS) as described in Shchepetkin and McWilliams (1998, 2003, 2005) with a horizontal resolution of 4 km coupled to the Carbon, Ocean Biogeochemistry, and Lower Trophics (COBALT) ecosystem model (Stock et al., 2014). This coupled model captures the spatial pattern and magnitude of mesoscale variability within the domain (Friedrich et al., 2021, 2024).

This regional model was then nested within output of the Coupled Model Intercomparison Project 6 (CMIP6) employing the Community Earth System Model version 2 (CESM2) detailed by Danabasoglu et al. (2020) using three different greenhouse gas scenarios (SSP1-2.6, SSP2-4.5, SSP3-7.0) for the time period 2000–2100. A total of three downscaling simulations were conducted for the SSP3-7.0 scenario to account for interannual and decadal variability employing output from the CESM2 Large Ensemble (Rodgers et al., 2021). The resulting downscaling simulations maintain the large-scale trends and interannual variability found in CESM2 while well representing the regional dynamics and short-term variability of our domain. More details on the methodology and performance of the downscaling can be found in Friedrich et al. (2024).

The model has been extensively used to explore physical processes (Matthews et al., 2012; Azevedo Correia de Souza et al., 2015; Azevedo Correia de Souza and Powell, 2017; Partridge et al., 2019) as well as biogeochemical dynamics (Friedrich et al., 2021, 2024; Feloy et al., 2024; Hošeková et al., 2025) around the MHI. The various aspects of the model's performance have been evaluated in those studies and others. For the current paper, we will therefore limit our model validation to the three variables of interest: T, $[H^+]$, and $[O_2]$. Vertical profiles are derived for the Station ALOHA location (Karl and Church, 2018) by extracting monthly-mean model data for all five simulations at the corresponding model grid point for the time period where observations from the Hawai'i Ocean Time-Series (HOT) program and simulations overlap (2001–2024). Using all five simulations as well as a temporal resolution similar to HOT ($\sim$ monthly) allows us to also compare the spread for both data sets. Observed and simulated vertical profiles for the Station ALOHA location are generally in good agreement (Fig. A1). The decrease of the seasonal temperature amplitude with depth is well captured by the model. For $[H^+]$, an increase in the data spread with increasing depth can be seen. This is caused by the fact that $[H^+]$ has a higher sensitivity to changes in dissolved inorganic carbon (DIC) for higher $[H^+]$ (higher DIC) concentrations such that for the conditions shown here the same change in DIC results in 2–3 times the change in $[H^+]$ at 500 m as compared to the surface. This feature is well captured by the model. Simulated $[O_2]$ exhibits a sub-surface maximum that is slightly deeper than the observed one. Below $\sim$ 550 m the model's ability to capture the vertical extent and magnitude of minimum $[O_2]$ values is limited. One reason for this can be found in the vertical resolution of the regional model that is in the order of $\sim$ 100 m around those depths. This is further complicated by the fact that the regional model is nested in a global climate model that are known to have difficulties representing oxygen minimum zones due to a lack of resolution and insufficient process parameterizations.

The temporal evolution of observed and simulated surface values of T, $[H^+]$, and $[O_2]$ is also in good agreement (Fig. A2). For T, it can be seen that the observed mean and seasonal cycle amplitude are well captured by the model. The modeled mean slope of T over the 2001–2024 period is lower than the observed one (dashed lines in Fig. A2a and Table A1). However, the range of slopes simulated by the five model runs indicates that the time period is simply too short and governed by interannual-to-decadal variability in T rather than a distinct warming signal. Simulated mean $[H^+]$ are slightly lower than observations. The upward trends in model and observations are in very good agreement and are almost identical across all five simulations. Observed $[O_2]$ are about 2 $\mu mol\,kg^{-1}$ higher than simulated for the 2001–2024 period. The simulated $[O_2]$ seasonal cycle amplitude and decrease agree reasonably well with the observations. The model spread in $[O_2]$ decrease is fairly large, indicating once again the impact of natural variability.

2.2 Definition of compound events and metrics

Compound events (CEs) are multiple extreme events that occur at the same time in the same location (Gruber et al., 2021). Biological consequences of extreme events depend on the nature of the events and the species considered and can therefore not be inferred directly. Rather, extreme events can be regarded as a probability of harmfulness (Hauri et al., 2024) and the most relevant characteristics of extreme events are their duration, intensity, severity, and other factors. These parameters depend on the local trend of the variable considered as well as the local amplitude of its natural variability envelope.

In our present study we focus on CEs with respect to high T, high $[H^+]$, and low $[O_2]$ in the upper 600 m. This choice is motivated by our intention to analyze extreme-event characteristics with a focus on depth layers that are subject to the strongest anthropogenic changes and are home to corals, high concentrations of plankton, and higher predators. The choice of stressors follows previous studies (Gruber et al., 2021; Hauri et al., 2024; Wong et al., 2024) and the general notion that these three stressors are among the most concerning in ocean environments. Given that pH is defined on a logarithmic scale, our calculations use $[H^+]$ instead to make the applied extreme-event statistics consistent for all three variables. We define an event for extremely high T and $[H^+]$ as an exceedance of the 99th percentile using the years 2005–2020 as a baseline period. Extremely low $[O_2]$ is defined as below the 1th percentile. Our choice of a fixed, relative threshold is motivated by the absence of absolute thresholds for the considered variables. An advantage of using a relative threshold based on the variables distributions is given by the fact that that all variables are treated statistically equal when it comes to the definition of what constitutes an "extreme event". Disadvantages of using a fixed relative threshold are that this approach does not take into account potential adaptation to trends as well as that extreme events that are – by definition – rare can turn into permanent features. (See Amaya et al., 2023 for a discussion of this issue in the context of marine heat waves.)

We consider five different depth layers for our analysis: 0–50, 50–100, 100–200, 200–400, and 400–600 m. The upper two layers cover the near-surface/upper euphotic zone with a separation at 50 m representing the annual-mean of the mixed layer depth (MLD). The third layer captures the lower euphotic zone, respectively. The lower two layers represent the subsurface and the lower levels of diel vertical migration. T and $[O_2]$ are part of the model output. $[H^+]$ is calculated from the model output variables T, salinity, dissolved inorganic carbon, and total alkalinity for every grid point using PyCO2SYS (Humphreys et al., 2022). T, $[H^+]$, and $[O_2]$ are vertically averaged over the depth bins to calculate reference statistics as well as event characteristics. We acknowledge that all three variables can be subject to substantial vertical gradients within the depths considered, rendering a depth-averaged perspective somewhat debatable. Ideally, calculations of thresholds, anomalies, and CECs should be carried out for every model grid point. But given the number of grid points in our high-resolution model and the length of the simulations, this approach would not be computationally feasible. Using isopycnals instead of depth bins might appear to be a more appropriate option since isopycnals are more representative of physical processes as well as different water masses. However, isopycnals disappear and reappear seasonally and as a consequence of long-term warming. This makes them an inconvenient choice for interpreting results with respect to potential habitat changes since habitats are typically defined by actual water depths. A similar caveat applies to MLD. In our domain, MLD varies seasonally between ~ 10 and ≥ 100 m. Spatial variations – driven by fronts and mesoscale eddies – are of similar magnitude across scales of ≤ 100 km. Based on this reasoning, we believe that – despite the limitations – our vertical partitioning constitutes a good compromise to present our results in an accessible and usable way to the reader.

The ocean around Hawai'i is home to considerable mesoscale and tidal activities. Both processes can substantially affect the local natural variability of T, $[H^+]$, and $[O_2]$. For our study, we will explicitly take into account both sources of variability. For each model grid point and each of the four depth bins, we use two different datasets to determine threshold values for T, $[H^+]$, and $[O_2]$, respectively:

1. In order to capture mesoscale variability, daily-mean values are used: Allowing for a five-year spin-up period for all runs, we use detrended daily-mean values for the time period 2005–2020. To increase statistical robustness, we concatenate four of the five simulations. Please note that the SSP1-2.6 and SSP2-4.5 simulations are identical in the "historical" part until the end of the year 2014. This concatenation allows for a total of 23 400 daily averages for each model grid point and depth bin. It should be noted that we consider the local seasonal amplitude as part of the natural variability envelope and do not remove a seasonal cycle from the dataset. Thresholds are then calculated from the first ($[O_2]$) and 99th (T and $[H^+]$) percentile.

2. In addition, 1 year of hourly output is used to assess the impact of tidal and other short-term variability on threshold values. For every grid point and depth bin, a total of 8800 hourly snapshots are detrended and high-pass filtered with a cutoff of 48 h. Tidal thresholds are then found from the first ($[O_2]$) and 99th (T and $[H^+]$) percentile.

In a final step, the threshold values calculated in steps 1 and 2 are compared and the larger amplitude of the two is chosen as the natural reference variability for this grid point and depth bin. The resulting threshold values as well as their spatial patterns are presented and discussed in Sect. 3.2.

Using the threshold values, CECs are calculated for every grid point and depth bin using daily-mean model output. Our calculations include the number of event days per year, duration, intensity, and severity. The duration of a compound event is defined as the number of consecutive days for which thresholds are exceeded for all three variables. The individual mean intensities for the three variables are calculated by averaging the amount the daily value exceeds the threshold over the course of the compound-event duration. In the case of temperature, this is given by the following equation:

$$I_{\mathrm{T}} = \langle T - T_{\mathrm{threshold}} \rangle \tag{1}$$

Here, $T_{\mathrm{threshold}}$ denotes the local threshold value for temperature and $\langle \ldots \rangle$ indicates the temporal averaging over the duration of the event.

Following Wong et al. (2024), a combined intensity can then be calculated from the normalized individual intensities. The normalized intensity (I') is the ratio of how far the threshold has been exceeded versus how far the threshold is from the typical conditions. For temperature (I'_{T}) the calculation takes the following form:

$$I'_{\mathrm{T}} = \frac{\langle T - T_{\mathrm{threshold}} \rangle}{T_{\mathrm{threshold}} - T_{50\,\%}} \tag{2}$$

where $T_{50\,\%}$ indicates the local value of the 50th percentile. Accordingly, the other normalized intensities are defined as:

$$I'_{[\mathrm{H}^+]} = \frac{\langle [\mathrm{H}^+] - [\mathrm{H}^+]_{\mathrm{threshold}} \rangle}{[\mathrm{H}^+]_{\mathrm{threshold}} - [\mathrm{H}^+]_{50\,\%}} \tag{3}$$

$$I'_{[\mathrm{O}_2]} = \frac{\langle [\mathrm{O}_2] - [\mathrm{O}_2]_{\mathrm{threshold}} \rangle}{[\mathrm{O}_2]_{\mathrm{threshold}} - [\mathrm{O}_2]_{50\,\%}} \tag{4}$$

The combined intensity (I_{com}) is then calculated as:

$$I_{\mathrm{com}} = \sqrt{\left(I'_{\mathrm{T}}\right)^2 + \left(I'_{[\mathrm{H}^+]}\right)^2 + \left(I'_{[\mathrm{O}_2]}\right)^2} \tag{5}$$

The combined intensity is dimensionless and can be regarded as a measure of how far the considered extreme state is outside the natural variability range. Combined intensity and duration are then combined into severity, defined as the product of combined intensity and duration. This approach is similar to, e.g., degree heating weeks used as a metric for the severity of coral bleaching (McClanahan, 2022) and expresses the fact that a weaker event over a long period of time may have the same effect as a strong event over a short period. The combined severity in our calculations is in unit of days.

Given the length of our simulations and the fact that calculations are conducted at every grid point and depth bin, CECs calculated from daily averages are averaged for each year, and our analysis will mainly focus on annual-mean durations, combined intensities, and severities. However, one decade of daily CECs will be presented to explore propagation characteristics in space and time.

The magnitudes and spatial patterns of CECs that might ultimately determine local ecosystem impacts depend mainly on natural-variability envelopes and anthropogenic trends of the variables considered. In order to separate the individual effects of these two drivers, we carry out two additional calculations of CECs:

1. CECs are calculated for every grid point and depth bin using daily-mean model output but domain-mean (depth-dependent) thresholds for T, $[\mathrm{H}^+]$, and $[\mathrm{O}_2]$, respectively.

2. CECs are calculated for every grid point and depth bin using spatially varying thresholds but domain-mean (depth-dependent) trends for T, $[\mathrm{H}^+]$, and $[\mathrm{O}_2]$, respectively. In this case, a second order polynomial is fit to each of the three variables for every grid point and depth bin. This fit is subtracted from the local timeseries and the domain-averaged fit is added.

The spatial patterns of CECs calculated for domain-average trends and domain-average thresholds, respectively, are then compared to the reference CECs to determine the individual effects of spatially varying trends and thresholds.

2.3 Sub-domains

As discussed in the Introduction, the Hawai'i domain is home to substantial mesoscale variability. However, this mesoscale variability is unevenly distributed with a clear focus on the western (leeward) side of the islands as indicated by the spatial pattern of mean eddy kinetic energy shown in Fig. 1 (contour lines). Certain coastal regions can be subject to significant tidal variability. To account for the inhomogeneity of our domain, we define three distinct sub-domains for our analysis and spatial averaging of CECs: a leeward sub-domain, a windward sub-domain, and a near-shore sub-domain (black lines in Fig. 1). The wind- and leeward sub-domain follow the ones presented in Matthews et al. (2011). For the near-shore sub-domain we chose grid cells within ~ 30 km of the coast as well as shallow areas such as the Penguin Banks.

3 Results and discussion

Compound event metrics such as duration, intensity, and severity are typically considered as a probability of harmfulness. Local CECs ultimately depend on the combination of two parameters: the local trends and the local envelope of natural variability. As a consequence, we will first analyze domain-wide trends as well as region-specific differences and examine the spatial patterns of the natural-variability envelope for the different depth bins. This will be followed by an in-depth analysis of CECs.

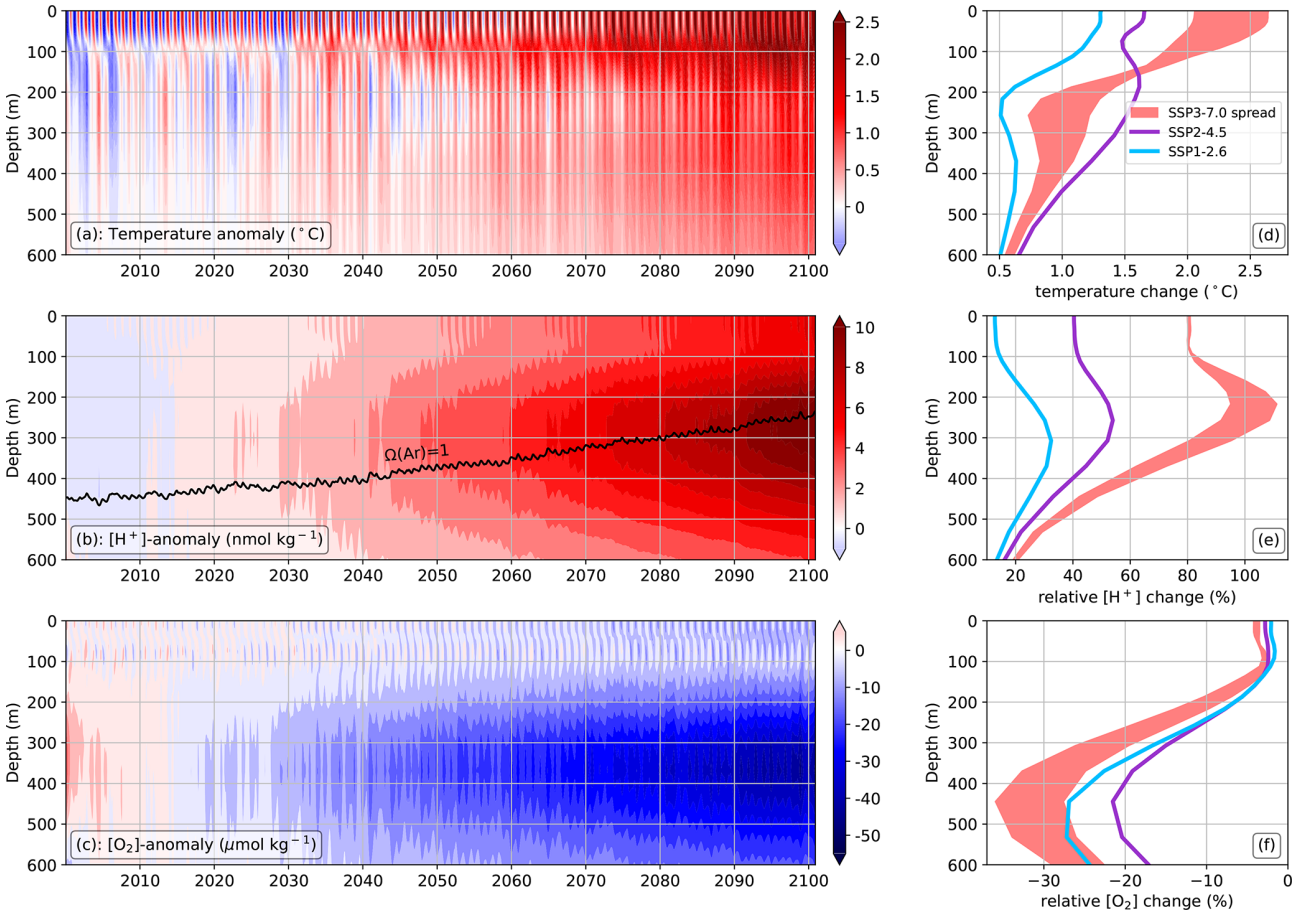


Figure 2. Domain-wide anomalies with respect to 2005–2020 mean in temperature (T), hydrogen ion concentration ($[H^+]$), and oxygen concentration ($[O_2]$). **(a)**: Domain-mean anomaly evolution averaged for all three SSP3-7.0 simulations (°C). **(b)**: Same as **(a)** for $[H^+]$ ($nmol\,kg^{-1}$). Black line indicates domain-averaged aragonite saturation horizon ($\Omega(Ar) = 1$). **(c)**: Same as **(a)** for $[O_2]$ ($\mu mol\,kg^{-1}$). **(d–f)**: Domain-averaged relative anomalies (absolute anomaly for T) averaged for years 2091–2100. Scenarios as indicated in panel **(d)**. The spread of the three SSP3-7.0 simulations is given by the red envelope. See Sect. 3 for details.

3.1 Anthropogenic trends

Increasing GHG concentrations are projected to have substantial impacts on temperature, carbonate chemistry, and O_2 concentrations across the world's ocean (Kwiatkowski et al., 2020) as well as the Hawai'i domain over the course of the 21st century (Fig. 2). The strongest temperature increase is found near the surface with a warming of ∼2.2–2.7 °C in the SSP3-7.0 scenarios (Fig. 2a and d). Depths of 200–400 m are projected to experience ∼0.7–1.3 °C warming by the year 2100. $[H^+]$ increases by ∼80 % at the surface (SSP3-7.0) and more than doubles at depths of around 200–400 m (Fig. 2b and e). At 100 m water depth the absolute, domain-average, end-of-century $[H^+]$ anomalies are in the order of 1 $nmol\,kg^{-1}$ (SSP1-2.6) to 5.25 $nmol\,kg^{-1}$ (SSP3-7.0). When comparing these values to the shapshot of $[H^+]$ shown by Fig. 1, it becomes apparent that the natural variability range of ∼1–2 $nmol\,kg^{-1}$ induced by mesoscale activity has a similar magnitude as the end-of-century $[H^+]$ anomalies in the lower emission scenarios and still reaches ∼20 %–40 % of the anomalies simulated for SSP3-7.0 at this depth. Consequently, natural variability has to be taken into account when evaluating trends. The simulated aragonite saturation horizon is found at a depth of around 450 m at the beginning of the 21st century – in good agreement with Station ALOHA observations (Fig. A1d). As a result of a decrease in carbonate ion concentration, the saturation horizon shoals from 450 m to about 250 m by the year 2100 (Figs. 2b and A1d). However, the local depth of the saturation horizon is highly variable across the domain and strongly influenced by mesoscale activity uplifting/suppressing isopycnals. O_2 concentrations at the surface decrease by ∼8 $\mu mol\,kg^{-1}$ (corresponding to ∼5 %) by the year 2100 as a result of the decrease in O_2 solubility associated with the warming. Sub-surface $[O_2]$ decrease is larger, reaching a maximum relative loss of 30 % at depths of ∼400–600 m (Fig. 2c and f). Changes projected by the lower emission scenarios are generally smaller (Fig. 2d–f) with the exception of sub-surface

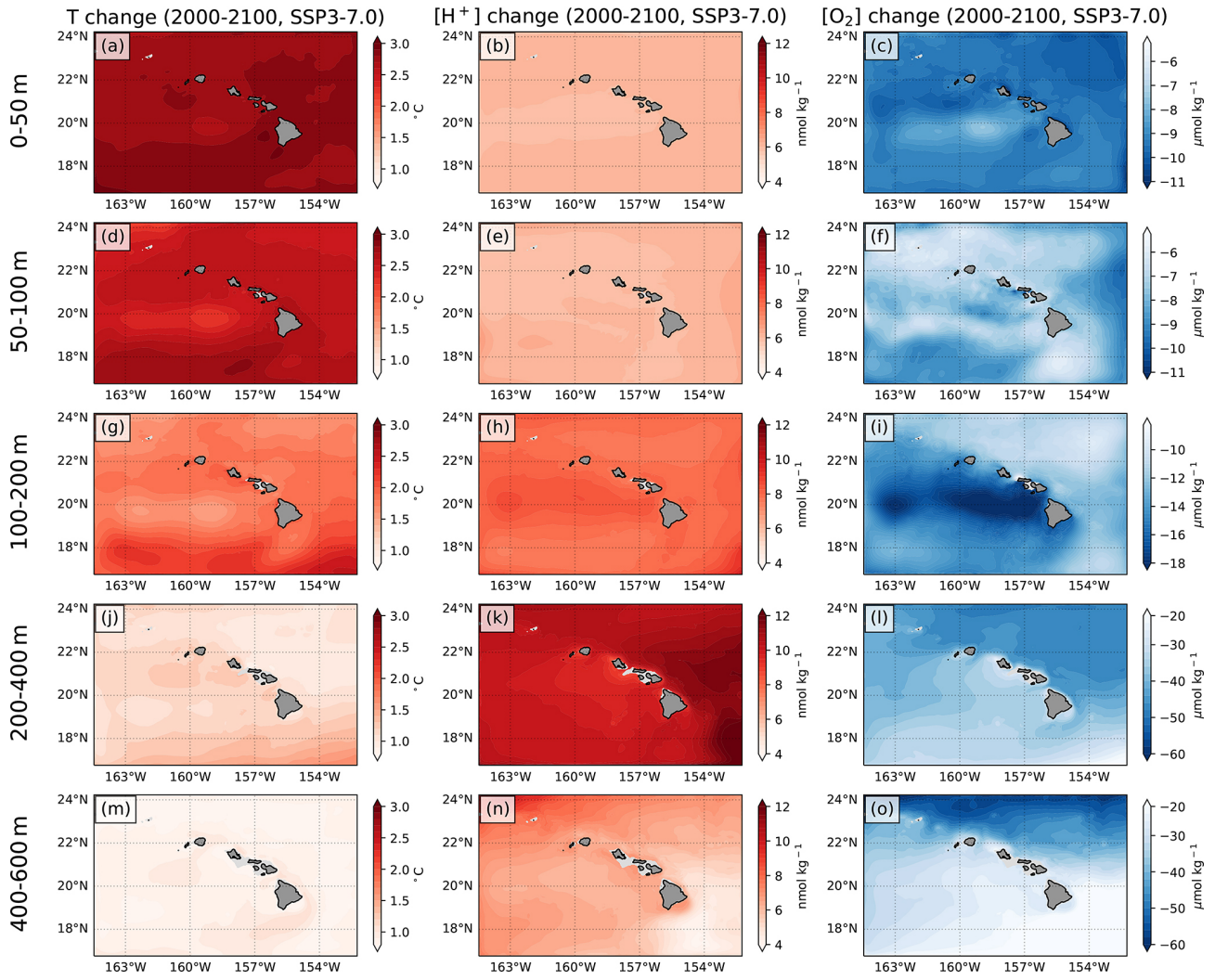


Figure 3. Projected changes in temperature (T), hydrogen ion concentration ($[H^+]$), and oxygen concentration ($[O_2]$) across the 21st century for the SSP3-7.0 scenario. Left column: changes in T (°C), middle column: changes in $[H^+]$ (nmol kg^{-1}), and right column: changes in $[O_2]$ (µmol kg^{-1}). Depth bins as indicated on the left. Individual colorbar ranges for were used for different depth bins in the right column for clarity. Please refer to text for calculation of projected changes.

temperature in the SSP2-4.5 simulation. However, only one simulation per scenario was conducted for SSP1-2.6 and SSP2-4.5, respectively, impeding the assessment of the effect of interannual-to-decadal variability on this result.

Changes induced by warming and uptake of atmospheric CO_2 are not uniform across our domain. Spatial inhomogeneities in T, $[H^+]$, and $[O_2]$ changes will affect CECs. In order to evaluate these inhomogeneities, we calculate the overall projected change for all three variables for the 2000–2100 time period. We use annual-mean values of T, $[H^+]$, and $[O_2]$ for all grid points, depth bins, and all three SSP3-7.0 simulations and apply a second order polynomial fit to smooth the data and to calculate anomalies for the 21st century. In a second step, the anomalies are averaged across all three SSP3-7.0 simulations to account for interannual-to-decadal variability. It can be seen that changes are the most homogeneous in the 0–50 and 50–100 m depth bins (Fig. 3a–f). Domain-wide differences in the surface depth bin in projected T changes are in the order of ± 0.15 °C and ± 10 % (± 20 %) for $[H^+]$ ($[O_2]$). While it would go beyond the focus of the present manuscript to investigate the drivers of spatial differences in trends in detail, it should be noted that inhomogeneities in the upper 200 m are clearly related to areas of mesoscale activities and the pathways of cyclonic and anticyclonic eddies to the west of the islands (Calil et al., 2008; Yoshida et al., 2010).

Relative differences in changes to T, $[H^+]$, and $[O_2]$ are substantially larger in the two depth bins below 200 m. However, mesoscale activity plays less of a role in shaping these patterns. At these depths, watermass characteristics such as

its age and propagation are major drivers of the pattern generation. The main watermasses involved around those depths are Subtropical Mode Water (STMW), North Pacific Intermediate Water (NPIW), and North Equatorial Pacific Intermediate Water (NEqPIW) (Bostock et al., 2010; Behrens et al., 2018). NEqPIW is a mix of Antarctic Intermediate Water and Pacific Deep Water and its lower $[O_2]$ (Bostock et al., 2010) and the radiocarbon signature indicate a substantially older and less ventilated watermass (Cross et al., 2015) as compared to NPIW. Due to the geometry of the subtropical overturning cell the northern part of our domain is more dominated by NPIW below 400 m whereas the southern part is more under the influence of NEqPIW. As a consequence, the southern parts are less rapidly affected by surface warming and CO_2-uptake. Hence, climate-change induced anomalies in carbonate chemistry and $[O_2]$ at these depths are generally larger in the northern part of our domain compared to the south.

3.2 Spatial patterns of natural variability

The Hawai'i domain is home to substantial mesoscale and submesoscale activity, in particular to the west of the islands (Calil et al., 2008; Yoshida et al., 2010; Azevedo Correia de Souza et al., 2015). Mesoscale eddies can suppress and uplift isopycnals acting on the strong vertical gradients of T, $[H^+]$, and $[O_2]$. Lateral circulation induced by eddies can advect T, $[H^+]$, and $[O_2]$ across horizontal gradients. Both of these processes can generate substantial natural variability in T, $[H^+]$, $[O_2]$, and other variables in regions of eddy activity.

Eddy-driven variability has a strong impact on the magnitudes and spatial patterns of the natural-variability threshold derived for T, $[H^+]$, and $[O_2]$ (Fig. 4). Anti-cyclonic eddies deepen isopycnals and can lead to episodes of strong natural warming mainly in the southwest of the domain, resulting in a local warming threshold 2–3 times as high as in the eastern part (Fig. 4g and j). Cyclonic eddies, on the other hand, uplift isopycnals and can create episodes of naturally high $[H^+]$ and low $[O_2]$, respectively for depth bins ≤ 200 m. As a consequence, the threshold amplitude for high $[H^+]$ and low $[O_2]$ in the regions of strong cyclonic eddy activity (central, western domain) is 2–3 times higher than in the northern and eastern part of the domain. It must be noted that due to these dynamics, natural variability maxima for high T on the one hand and high $[H^+]$ with low $[O_2]$ on the other hand do not fully overlap. The effect of cyclonic eddy activity can also be identified at the surface (0–50 m, Fig. 4a–c). However, near the surface, the seasonal cycle is also an important player. Seasonal warming leads to an increase in the dissociation of water molecules resulting in a higher $[H^+]$. At the same time, $[O_2]$ solubility decreases, leading to lower $[O_2]$ near the surface (see also Fig. A2). The amplitude of seasonal warming/cooling is larger in the north than the south, leading to meridional gradients in the thresholds that are superimposed on the regions of highest mesoscale activity.

The southern region of our domain is characterized by a meridional gradient in watermass ventilation in the 400–600 m depth bin. The more southerly and less ventilated NEqPIW is naturally high in $[H^+]$ and low in $[O_2]$ compared to the more northerly located NPIW. Lateral advection induced by anticyclonic eddies spinning off the Island of Hawai'i can entrain these waters northward, resulting in larger natural variability in these regions (Fig. 4m–o).

In addition to eddy-induced natural variability, the Hawaiian archipelago is also an important site of barotropic tidal dissipation (Merrifield and Holloway, 2002; Rainville et al., 2010). This dissipation is a daily process and can induce vertical heaving and mixing of biogeochemical tracers and temperature in the sub-surface, near-shore environment. Our numerical approach enables us to separate the effects of tidal (and other short-term) variability from (sub-)mesoscale variability and compare the magnitudes of the thresholds that each of these sources of natural variability would result in. (Please see Sect. 2.2 for details on the calculation.) This allows us to identify regions where the (oftentimes overlooked) effect of tides will become relevant for projecting CECs; and to understand how increased natural variability added by tides may potentially delay the onset of CEs and weaken their combined intensities and severities.

As a metric to identify such regions, we choose the ratio between the local threshold-amplitudes calculated from hourly versus the local threshold-amplitudes calculated from daily-mean values. (See Sect. 2.2 for details.) Fig. 5 illustrates this ratio for the most affected depth bin of 100–200 m. As expected, natural variability created mainly by mesoscale activity (and represented by daily-mean values) exceeds tidal variability in almost all open ocean areas. However, certain coastal areas exhibit ratios of ~ 2, meaning that the threshold amplitude for an extreme event is twice as high as it would be when tidal variability is not considered. The effect of this increased natural variability envelope is particularly important for considering CEs in nearshore coral reef ecosystems and will be discussed in Sect. 3.4.

In view of the strong effects of mesoscale activity and tides on local extreme-event thresholds, it must be emphasized that coarse-resolution global climate models are incapable of resolving or parameterizing these processes. As a consequence, the natural variability envelope of relevant variables simulated by global climate models tends to be unrealistically small, impeding a robust projection of CECs.

3.3 Projected compound event characteristics

The temporal evolution of atmospheric CO_2 concentrations differs substantially between different SSP scenarios, resulting in different impacts on T, $[H^+]$, and $[O_2]$ in particular near the ocean's surface. In the SSP3-7.0 scenario, atmospheric CO_2 continues to rise throughout the 21st century,

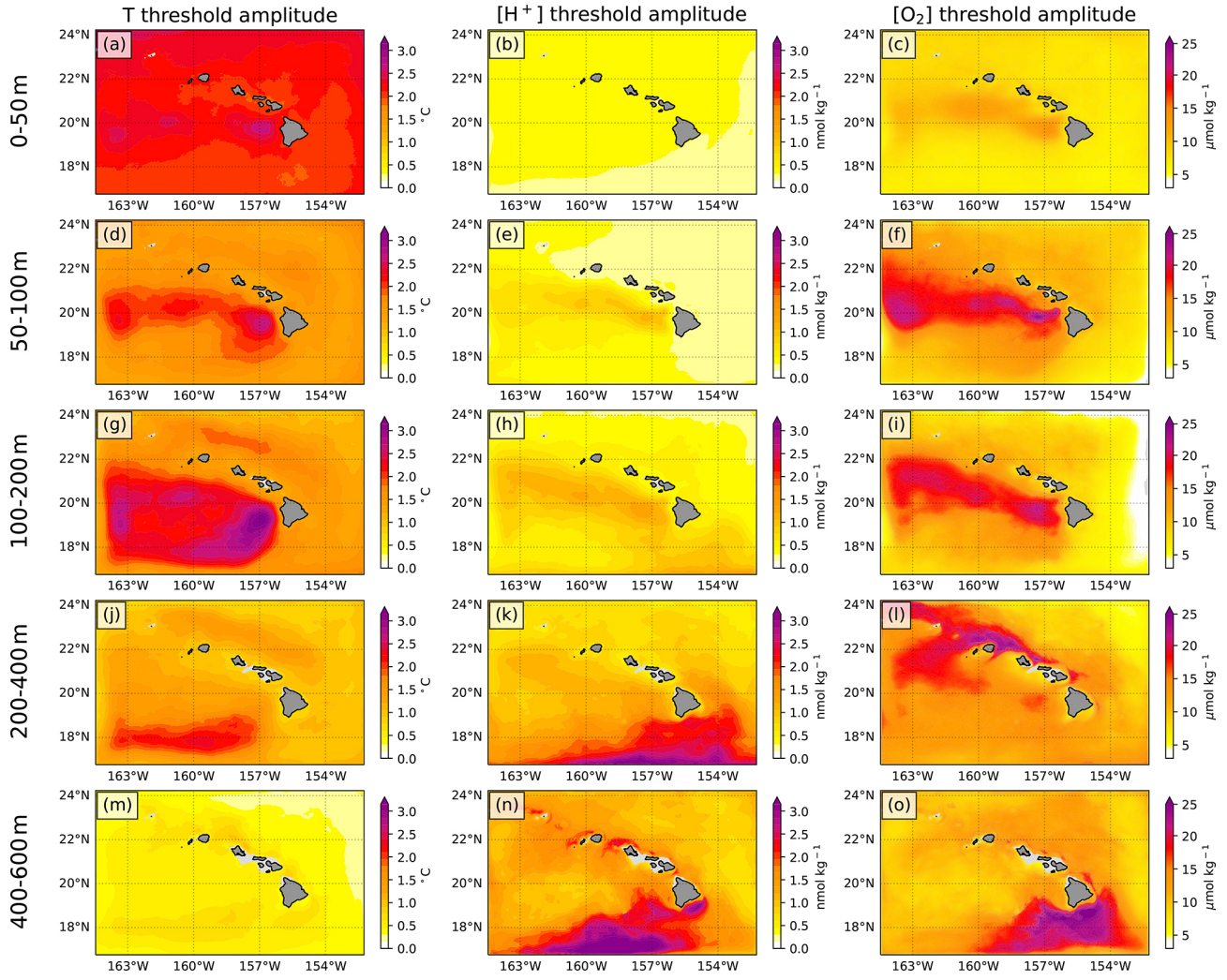


Figure 4. Threshold amplitudes for temperature (T), hydrogen ion concentration ($[H^+]$) and oxygen concentration ($[O_2]$). Left column: 99 percentile threshold amplitude for high T (°C), middle column: 99 percentile threshold amplitude for high $[H^+]$ (nmol kg^{-1}), and right column: 1 percentile threshold amplitude for low $[O_2]$ (µmol kg^{-1}). Depth bins as indicated on the left. Please refer to Sect. 2.2 for calculation of threshold amplitudes.

reaching a value of 871 µatm by the year 2100. The SSP2-4.5 scenario is characterized by a stabilization of atmospheric CO_2 concentration towards the end of the century, reaching a maximum of 603 µatm. In the SSP1-2.6 scenario, a maximum of 474 µatm is reached in the year 2063, followed by a decrease to 445 µatm by the year 2100.

Figure 6 depicts projected CE duration (shading), combined intensity (y-axis), and severity (circle sizes, see definition in Sect. 2.2) for the different simulations averaged for the depth bins and sub-domains (Fig. 1). The earliest onset of compound events is found in the 0–50 m depth bin, occurring in the 2020–2029 decade (Fig. 6a–c). Combined intensities are relatively uniform across the three sub-domains at this depth. Event duration (severity) is projected to be longer (higher) in windward areas and shortest (smallest) in nearshore regions. With respect to the three SSP scenarios, the largest difference between the different GHG scenarios in terms of CECs can be found at this depth level across all subdomains. In fact, combined intensities in the 0–50 m depth bin follow a near-linear relationship with atmospheric CO_2 concentrations (Fig. A3a–c). Duration and severity, however, are subject to a legacy effect and are still increasing substantially in the lower emission scenarios even with atmospheric CO_2 concentrations leveling off (SSP2-4.5) or decreasing (SSP1-2.6), respectively (Fig. A3). Approximately 94 % of the combined intensity is contributed by the exceedance of the $[H^+]$ threshold in the SSP3-7.0 scenario (see below). The exceedance of the $[H^+]$ threshold in the 0–50 m depth bin is projected to become a permanent feature around the year 2040 in all three SSP scenarios (Fig. A4b). In the case of T and $[O_2]$, it is the seasonal cycle that helps to keep the duration of threshold exceedance much shorter at this depth level

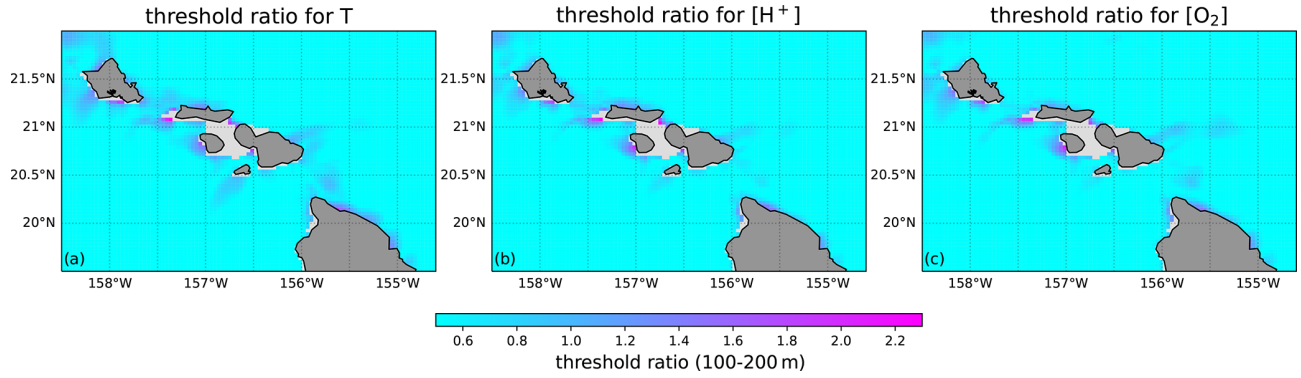


Figure 5. Ratios of threshold amplitudes based on hourly versus daily-mean data for temperature (T), hydrogen ion concentration ($[H^+]$), and oxygen concentration ($[O_2]$) for the 100–200 m depth bin. A ratio greater than one indicates that tidal and other short term variability exceeds variability calculated from daily-mean values. Left column: Threshold amplitude ratio for high T, middle column: threshold amplitude ratio for high $[H^+]$, and right column: threshold amplitude ratio for low $[O_2]$. Please refer to Sect. 2.2 for calculation of threshold amplitudes.

(see dashed lines in Fig. A4). By the middle of the century, approximately 20 % of the domain experiences threshold exceedance in the annual mean. By the end of the century, this value rises to ∼ 40 %–60 % depending on the emission scenario. It should be noted that the permanence of threshold exceedance does not affect the definition of intensity and corresponding CECs in our fixed threshold approach.

End-of-century projections of duration and combined intensity for the 0–50 m depth bin (Fig. 7a–d) reveal similar spatial patterns for the SSP1-2.6 and the SSP3-7.0 simulations. In both scenarios, the domain maxima of event duration are found in the windward area. Duration minima are located in the central leeward sub-domain in the pathway of cyclonic (cold core) eddies. The southern part of the leeward sub-domain that is home to anticyclonic (warm core) eddies is subject to CECs similar to those in the windward sub-domain.

The three depth bins that cover the 50–400 m ranges, respectively are characterized by substantially less pronounced CECs in the leeward sub-domain compared to windward and near-shore areas (Fig. 6d–l). Projected end-of-century combined intensities in the windward and near-shore areas are approximately twice as high as in the leeward area (Fig. 7e–p). In fact, large parts of the 100–200 m leeward sub-domain are projected to stay event-free even under the SSP3-7.0 scenario. The reason for this difference can be found in the generally higher extreme-event thresholds found in the leeward sub-domain at these depths (Fig. 4).

The longest event durations are found at the 400–600 m depth bin, reaching more than 250 d yr^{-1} (in the spatial average) in the SSP2-4.5 and SSP3-7.0 scenarios by the end of the century (Fig. 6m–o). Here, one can also find the least pronounced combined-intensity differences between sub-domains as well as between GHG scenarios. It should be noted, however, that our domain separation is not as valid at this depth level. Long duration and high combined intensity in the windward sub-domain are mainly driven by the northern and north-eastern areas (Fig. 7q–t) where event thresholds are comparably low (Fig. 4m–o) and trends in $[H^+]$ and $[O_2]$ are high (Fig. 3m–o). Duration and combined intensity are at their minimum in the south-eastern windward region, consistent with higher thresholds.

The 400–600 m depth bin is also subject to the strongest legacy effect of atmospheric CO_2 increase (Fig. A3). In fact, the strongest increase in CECs in the SSP2-4.5 scenario is found for atmospheric CO_2 values of > 550 µatm corresponding to the last 30 years when atmospheric CO_2 is starting to level off (Fig. A3m–o). Similarly, in the SSP1-2.6 scenario, values for duration and combined intensity more than double after atmospheric CO_2 has peaked. Accordingly, severity – being the product of the two – increases even more strongly (not shown).

To further investigate the role of local threshold amplitudes in creating the distinct spatial CEC patterns seen in Fig. 7 we carried out two additional CEC calculations using either domain-mean thresholds or domain-mean trends (Sect. 2.2). In order to quantitatively compare the arising patterns to the reference CECs, we determine pattern correlations and standard deviation ratios (Table 1). It becomes apparent that using a domain-mean trend for the calculations results in virtually identical spatial patterns of duration and combined intensity (and with it, severity). This means that it is mainly the spatial difference in event thresholds that is responsible for CEC differences across the domain.

In addition to duration, combined intensity, and severity, the composition of CEs with respect to the individual normalized intensities (see Eq. 2) – referred to as event flavors – can be relevant for species-specific responses. Our results reveal that CE flavors are projected to differ with depth bin, SSP scenario, between sub-domains, and for the time period considered (Fig. 8). In the upper 200 m, normalized $[H^+]$ intensities contribute between ∼ 85 % (SSP1-2.6) and

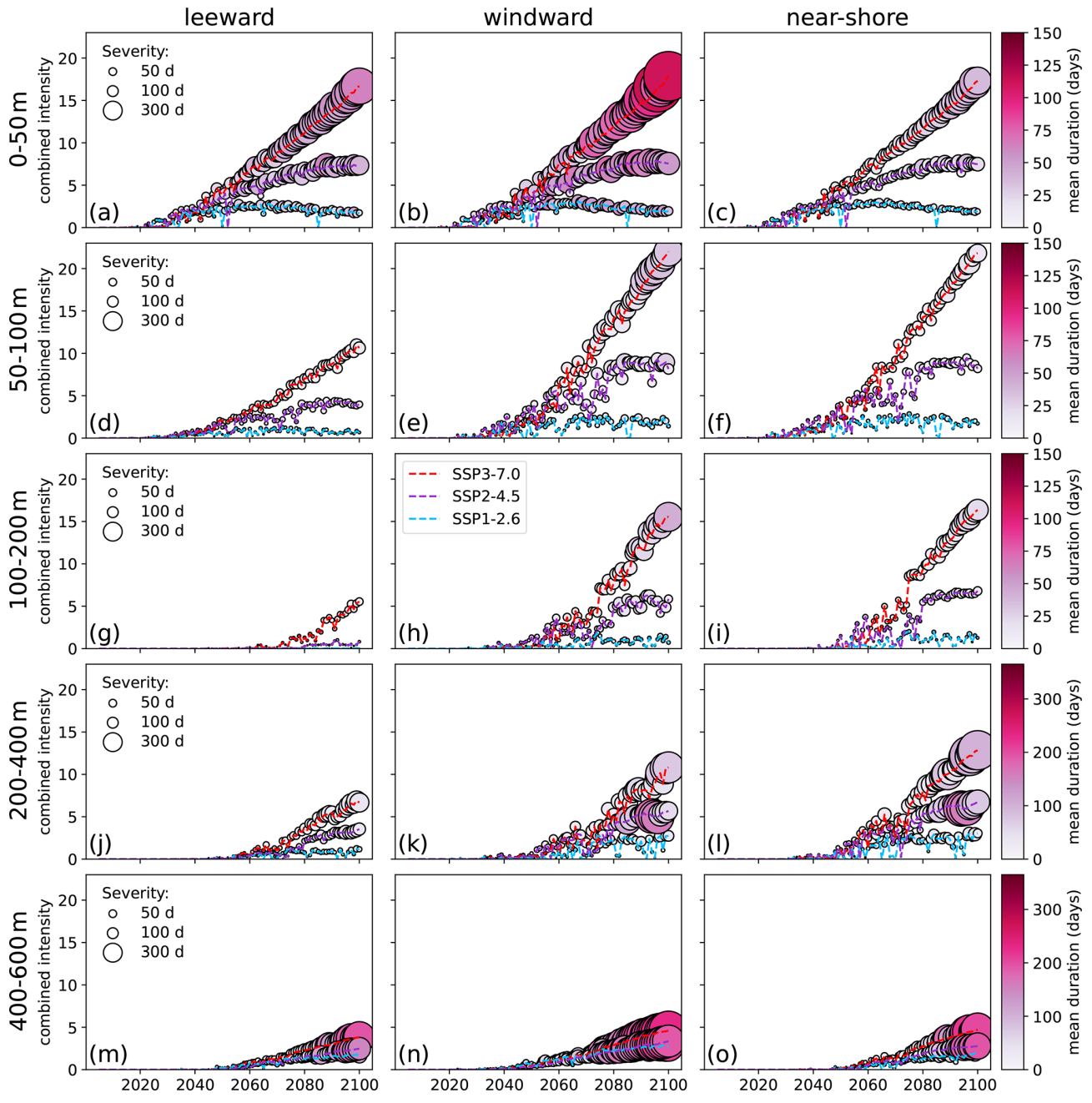


Figure 6. Projected compound event characteristics spatially averaged for leeward, windward, and near-shore sub-domains (black lines in Fig. 1) and different depth bins as indicated on the left. Colors: annual-mean duration (days), sizes of circles: annual-mean severity (days). Greenhouse gas scenarios are indicated by line colors. Red: mean of all three SSP3-7.0 scenarios, purple: SSP2-4.5 scenario, cyan: SSP1-2.6 scenario.

$\sim 95\,\%$ (SSP3-7.0) to the overall combined intensity, with T and $[O_2]$ adding $\sim 3\,\%$–$9\,\%$, respectively (Fig. 8a–i). Mid century (2050–2059) normalized intensities for 0–50 m $[H^+]$ reach values of ~ 5 in the SSP3-7.0 scenario (Table 2), meaning that $[H^+]$ are projected to exceed the 99th percentile threshold amplitude by a factor of five (Eq. 3). By the 2090–2099 decade, this factor is projected to increase to ~ 15. For the 100–200 m bin, the corresponding values amount to 0.55 and 9.08, respectively. This strong dominance of $[H^+]$ intensities means that the prominent flavor of CEs in this depth range is from ocean acidification.

At lower depth levels, low $[O_2]$ becomes substantially more relevant as a contributor to event flavors. At the 200–400 m depth bin, low $[O_2]$ contributes $\sim 13\,\%$–$17\,\%$ to the

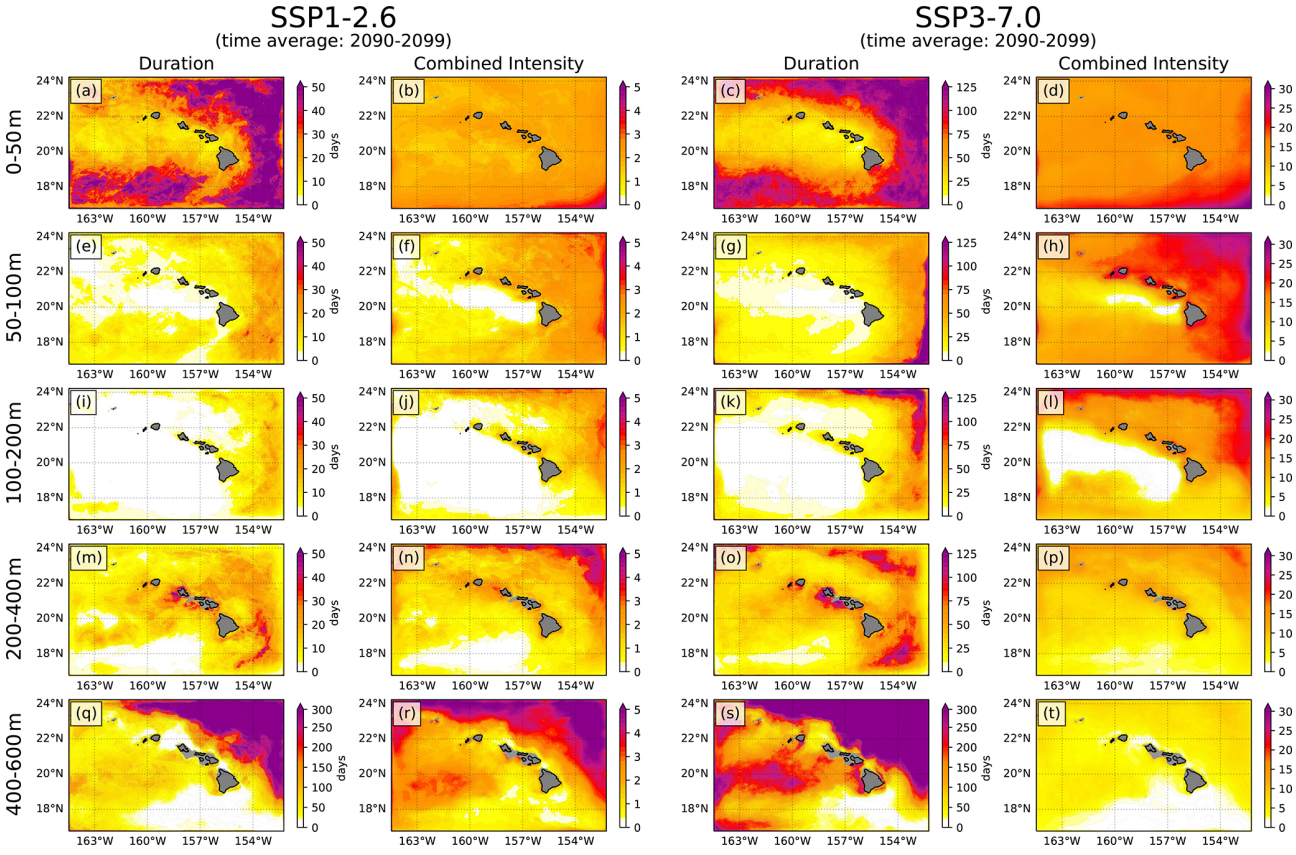


Figure 7. Projected compound event characteristics temporally averaged for years 2090–2099 for different depth bins. Columns 1 and 2: duration (days) and combined intensity for SSP1-2.6 simulation. Columns 3 and 4: duration (days) and combined intensity averaged for all three SSP3-7.0 simulations. Depth bins are indicated on the left. Severity was omitted to keep total number of panels manageable.

Table 1. Drivers of spatial patterns of compound event characteristics (CECs) averaged for the time period 2090–2099. Pattern correlation and standard deviation ratio for CECs calculated using domain-mean trend and domain-mean thresholds, respectively and reference CECs. See text for details and Sect. 2.2 and for calculation.

Depth	calculation method	pattern correlation for duration	standard deviation ratio for duration	pattern correlation for combined intensity	standard deviation ratio for combined intensity
0–50 m	domain-mean trend	0.99	1.00	1.00	0.97
	domain-mean threshold	0.95	0.79	−0.24	0.14
50–100 m	domain-mean trend	0.98	0.92	1.00	1.00
	domain-mean threshold	0.73	0.44	−0.27	0.16
100–200 m	domain-mean trend	0.94	1.37	0.99	1.08
	domain-mean threshold	0.63	0.15	−0.59	0.18
200–400 m	domain-mean trend	0.89	1.19	0.99	1.00
	domain-mean threshold	0.29	0.37	−0.32	0.15
400–600 m	domain-mean trend	0.92	0.95	0.91	0.92
	domain-mean threshold	0.83	0.61	0.53	0.36

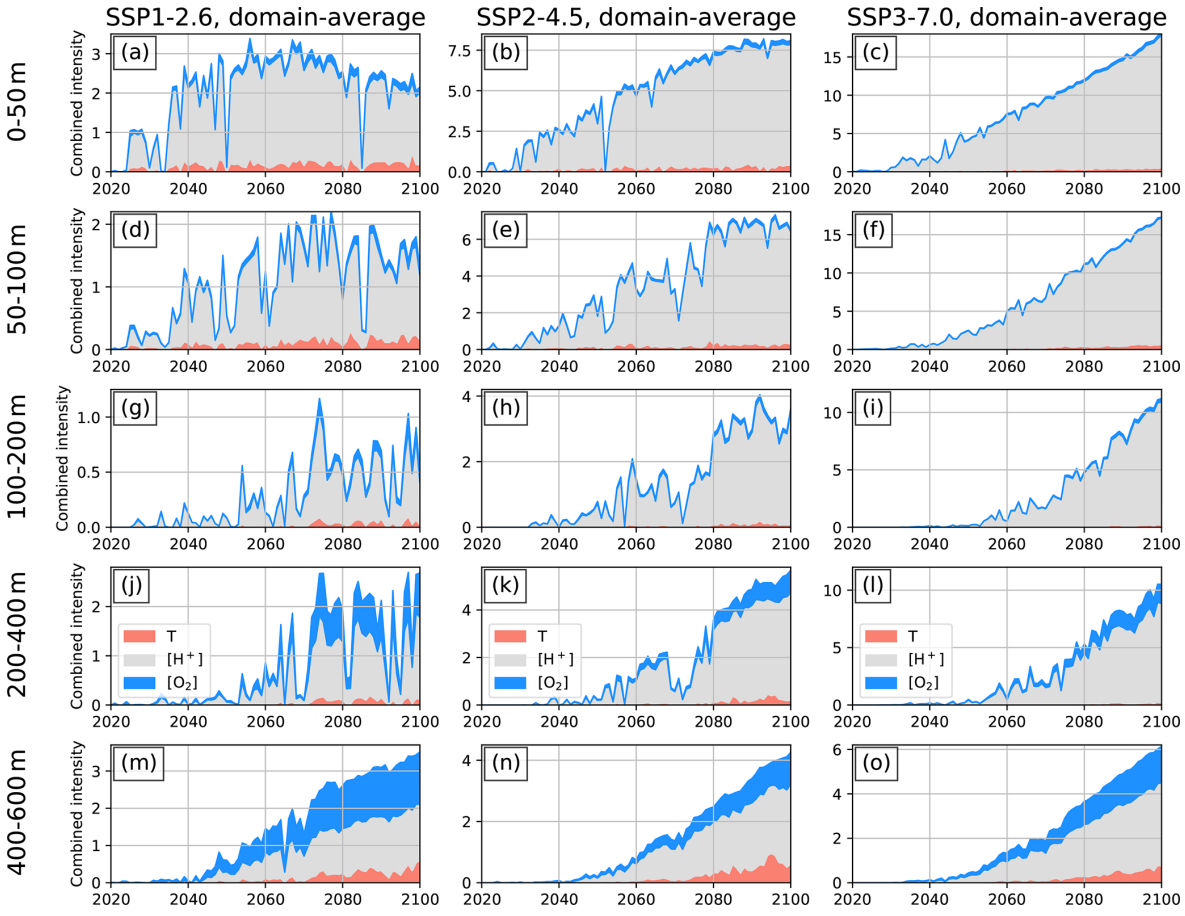


Figure 8. Projected domain-averaged composition of normalized compound event intensities (event flavors). Left column: SSP1-2.6 scenario, middle column: SSP2-4.5 scenario, right column: mean over all three SSP3-7.0 scenario simulations. Depth bins are indicated on the left.

overall combined intensity in the higher emission scenarios (Fig. 8k and l, Table 2). In the SSP1-2.6, scenario this rate roughly doubles to reach 29.4 % in the time-mean with strong interannual fluctuations (Fig. 8j). The role of low $[O_2]$ in shaping event flavors becomes even more important in the deepest layer (Fig. 8m–o). In the higher emission scenarios, the exceedance of the $[O_2]$ threshold contributes 23.8 % (SSP2-4.5) to 28.5 % (SSP3-7.0) to the overall combined intensities when averaged over the century. Normalized $[O_2]$ intensities slightly exceed the contribution by their $[H^+]$ counterparts in the SSP1-2.6 scenario in the middle of the century. Overall, high $[H^+]$ and low $[O_2]$ contribute almost equally to the CE flavors in this scenario.

3.4 Impact of tidal variability on compound event characteristics

Accounting for tidal (and other short-term) variability can result in substantially higher threshold amplitudes in certain near-shore areas (Sect. 3.2). Figure 5 shows that in hotspots of tidal variability in the 100–200 m depth bin, tidal threshold amplitudes can be approximately twice as high as those calculated from daily-mean values. The results presented have included tidal variability by using a combined threshold (Sect. 2.2) but do not allow for a clear attribution of local CECs to tidal variability. In order to elucidate the effect of tides, we use threshold amplitudes derived from daily-means and derived from hourly-means, respectively to calculate CECs for all simulations and all depth bins. The resulting CECs are then compared for every depth level and grid point to determine the location and magnitude of the effect of tidal variability on compound events.

The largest effects are only found in coastal locations at the 100–200 m level (Fig. 9). Using the local ratio between CECs calculated for the different thresholds for the end of the century in the SSP3-7.0 scenario (mean of all three runs) as a metric, it can be seen that in certain near-shore locations the number of event days per year (Fig. 9a) and the mean combined intensity (Fig. 9b) are strongly reduced when explicitly accounting for the larger natural-variability envelope created by tidal processes.

We choose three different locations near different islands to illustrate the effect of tidal variability for the SSP3-7.0 scenario: Mamala Bay at the south shore of O'ahu, the Penguin

Table 2. Projected domain-averaged composition of normalized compound event intensities (event flavors) for different depth bins and scenarios averaged for the time period 2050–2059 (2090–2099). See Sect. 2.2 and Eqs. (1)–(4) for calculation and Fig. 8 for temporal evolution. Normalized intensities are defined as the ratio of absolute intensity and the magnitude of the extreme-event amplitude and hence they indicate the factor by which the extreme-event threshold amplitude is being exceeded.

Depth	Variable	SSP1-2.6	SSP2-4.5	SSP3-7.0
0–50 m	T	0.17 (0.25)	0.21 (0.29)	0.17 (0.42)
	$[H^+]$	2.21 (1.86)	3.69 (7.41)	5.29 (15.43)
	$[O_2]$	0.11 (0.15)	0.14 (0.22)	0.12 (0.33)
50–100 m	T	0.08 (0.17)	0.17 (0.27)	0.12 (0.57)
	$[H^+]$	0.94 (1.23)	2.60 (6.42)	2.72 (14.80)
	$[O_2]$	0.05 (0.10)	0.08 (0.14)	0.07 (0.16)
100–200 m	T	0.01 (0.04)	0.03 (0.11)	0.01 (0.15)
	$[H^+]$	0.17 (0.45)	0.79 (3.10)	0.55 (9.08)
	$[O_2]$	0.02 (0.07)	0.05 (0.10)	0.02 (0.25)
200–400 m	T	0.01 (0.08)	0.03 (0.28)	0.02 (0.16)
	$[H^+]$	0.16 (0.98)	0.57 (4.12)	0.62 (7.24)
	$[O_2]$	0.06 (0.51)	0.10 (0.77)	0.10 (1.42)
400–600 m	T	0.05 (0.32)	0.04 (0.66)	0.06 (0.55)
	$[H^+]$	0.39 (1.53)	0.32 (2.32)	0.54 (3.38)
	$[O_2]$	0.43 (1.36)	0.10 (0.87)	0.21 (1.54)

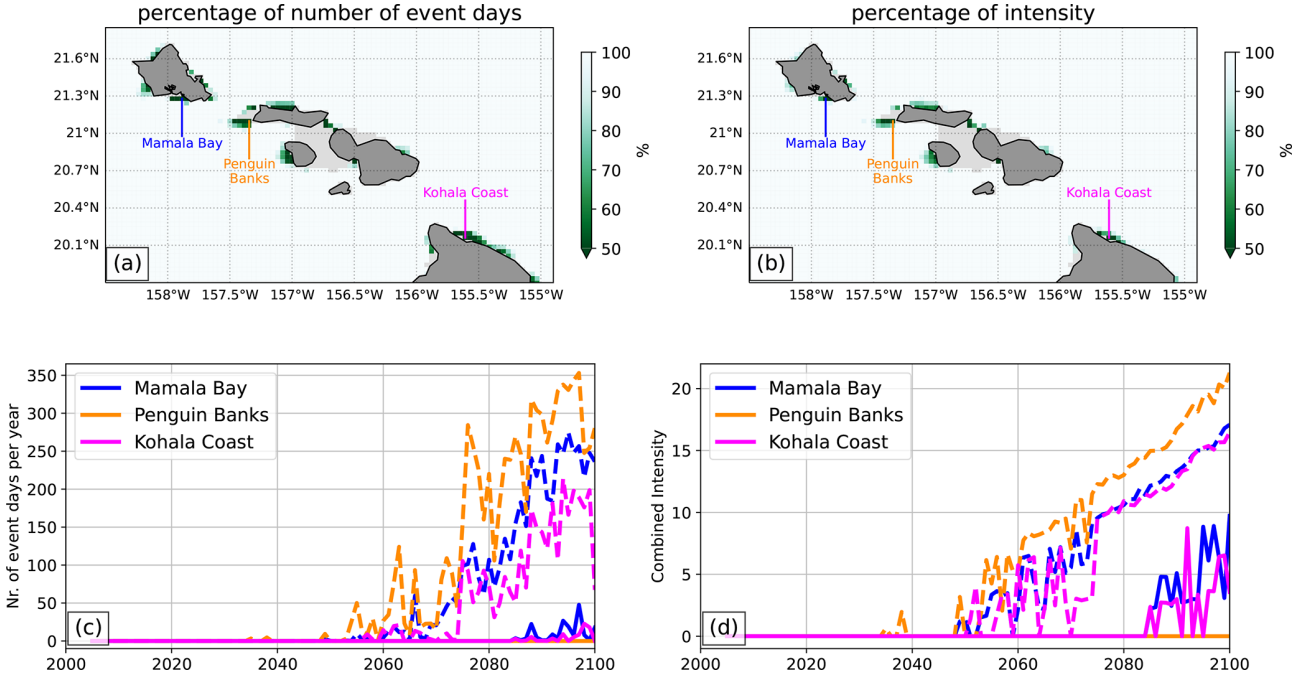


Figure 9. Effect of tides on compound event characteristics at the 100–200 m depth bin for the SSP3-7.0 scenario. A mean over all three SSP3-7.0 simulations is shown. **(a)**: Percentage of number of event days (%, averaged for time period 2090–2099) derived when tidal variability is taken into account as compared to thresholds solely based on daily-mean values. **(b)**: Same as **(a)** for combined intensity. **(c)**: Timeseries of number of event days per year (days) for grid points depicted in upper panels. Dashed lines: Event thresholds based on daily-mean data. Solid lines: Event thresholds based on hourly data. **(d)**: Same as **(c)** for combined intensity. See Sect. 3.4 for details and Sect. 2.2 for calculation.

Banks near Moloka'i, and the Kohala Coast near the Island of Hawai'i. In order to account for interannual-to-decadal variability, we employ a mean of CECs calculated for all three SSP3-7.0 simulations. Using threshold based on daily-mean, the onset of events is projected to occur in the 2050–2060 decade. For the end of the century, number of event days is in the range of 150–350 per year, depending on the exact location; combined intensities reach ∼ 16–21 (Fig. 9c, d; dashed lines). The projected CECs change drastically when the higher thresholds are used as a natural-variability reference. The onset of CECs is projected to occur ∼ 20 years later in the 2080–2090 decade for the locations near O'ahu and the Island of Hawai'i. The number of event days does not grow larger than $50\,\mathrm{d\,yr^{-1}}$ and combined intensities are projected to only reach about half the value seen for the daily-mean based thresholds. At the Penguin Banks location, no compound events are projected to occur at this depth level when using the higher thresholds.

With respect to other depth bins, it should be noted that the effect of tidal variability on CECs is negligible in above 100 m. At depths greater than 200 m, the effects are consistent with the ones presented for the 100–200 m bin but overall smaller (not shown).

Analyzing the SSP1-2.6 and SSP2-4.5 simulations, our results reveal that the spatial extent of the reduction of CEs is larger in the 100–200 m depth range compared to the SSP3-7.0 simulation (shown for SSP1-2.6 in Fig. A5a and b), which is consistent with the fact that anthropogenic trends are generally smaller in those scenarios. When daily-mean data are used as a baseline for natural variability, CEs with 100–200 event days per year are projected to occur for the three locations for SSP1-2.6 (Fig. A5c). When tidal variability is accounted for all three areas remain event-free throughout the century in the 100–200 m depth range.

While the spatial extent of the affected areas appears to be small, they are of particular relevance for the near-shore ecosystem and its protection. The Mamala Bay and the Kohala Coast are Fishery Management Areas. The Penguin Banks and other affected regions are part of the Hawaiian Humpback Whale National Marine Sanctuary. Other coastal areas subject to CE reduction highlighted by Fig. 9a and b are Marine Life Conservation Districts, Subsistence Fishing Areas, and other forms of Marine Protected Areas. The regions to the north of Moloka'i are home to strong productivity pulses as shown in the satellite records and model data (Feloy et al., 2024).

Our results highlight the potential role of tidal variability in priming local ecosystems for the various projected anthropogenic changes in general and CEs in particular, emphasizing the need for high-resolution regional modeling for robust projections of local climate change impacts.

3.5 Propagation characteristics in time and space

So far our analysis has focused on annual-mean CECs. Exploring timing and spatial propagation characteristics of CEs on shorter time scales will deepen our understanding of the nature of CEs and might allow for better predictability of future CEs. We calculate daily CECs for 20 years (2070–2089) as described in Sect. 2.2. Figure 10a–e shows the meridional average of the T intensity for 2080–2089 (first decade omitted for clarity). It can be seen that (in the meridional average) CEs follow a clear seasonality in the 0–50 m depth bin, peaking between August and October, controlled primarily by the seasonality of near-surface T. However, superimposed onto the seasonal pattern, we can identify patterns of westward propagation in CECs. These advective characteristics become substantially more pronounced in the deeper layers where seasonality plays a negligible role.

When averaging daily-mean sea-surface height (SSH) anomalies over the areas of daily CEs and plotting their cumulative distribution for the different depth bins (Fig. 10f, g) it can be seen that the distribution of CE-weighted SSH-anomalies differs substantially from the distribution of SSH-anomalies itself. Almost no CEs are associated with negative sea-surface height anomalies. In particular, on the leeward side of the islands, CEs occur in combination with positive SSH anomalies. Given also the advective nature of the CEs, we conclude that anti-cyclonic eddies are a major driver behind the local formation and propagation of CEs. Estimating the propagation speed from the slopes seen in Fig. 10c–e amounts to a value of $\sim 8\,\mathrm{cm\,s^{-1}}$ (see dashed lines in Fig. 10a–e). This value is consistent with observation-derived estimates for this latitude (Chelton and Schlax, 1996).

Anti-cyclonic eddies are characterized by a deepening of isopycnals. This process acts on the vertical gradients, bringing typically less acidic and more oxygenated but also warmer waters to deeper waters. And while high T plays only a negligible role in the composition of CEs compared to high $[H^+]$ and low $[O_2]$, it is ultimately the warming that is the determining factor in triggering CEs in the context of anti-cyclonic eddies. It should be noted, however, that when neglecting temperature and looking at high $[H^+]$ or low $[O_2]$ events individually or in combination, cyclonic eddies and the associated heaving of isopycnals would likely play an important role.

Combining these findings with the results of Sect. 3.2 and Fig. 4, it can be concluded that mesoscale eddies are both a blessing and a curse when it comes to CEs. On the one hand, the natural variability generated by eddies results in higher event thresholds, delaying the onset of CEs and decreasing their combined intensities. On the other hand, once mean values of T, $[H^+]$, and $[O_2]$ have changed sufficiently, eddies tend to generate CEs.

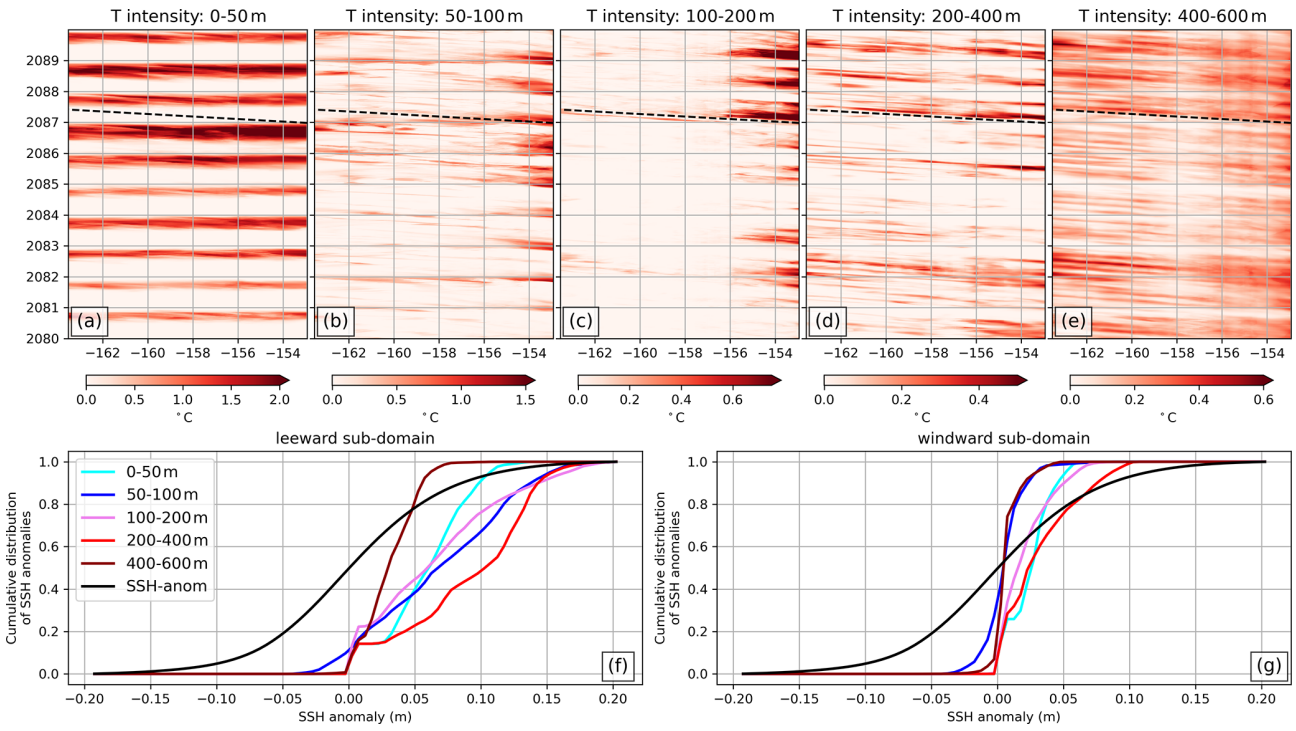


Figure 10. **(a–e)**: Hovmoeller plots of meridionally averaged temperature intensity (°C) of compound events for the depth layers given above the panels. Dashed line indicates the slope for a 8 cm s^{-1} westward propagation. **(f)**: Cumulative distribution of sea-surface anomalies associated with compound events on the leeward side. **(g)**: Same as **(f)** for the windward side.

3.6 Potential impacts for the Hawaiian marine ecosystem

Our results document that Hawaiian ecosystems in varying locations and depth levels are projected to be exposed to unprecedented extreme conditions with respect to high temperature, high ocean acidity, and low oxygen concentrations. Even though the consequences of compound events for organisms and ecosystems cannot yet be inferred directly, numerous studies have documented harmful effects of the stressors considered here for various organisms relevant for Hawaiian waters.

The Hawaiian archipelago has experienced multiple coral bleaching events (Jokiel and Brown, 2004; Bahr et al., 2015; Asner et al., 2022). Asner et al. (2022) examined a bleaching event in 2019 and showed that absolute local coral loss was highly correlated with the local duration and severity of the heat wave. However, the survey also exhibited that individual reef-scale factors substantially alter heat-induced coral mortality.

Corals responses to ocean acidification remain multifaceted and heavily genera dependent. Reduced calcification was shown by some studies (Chan and Connolly, 2013) (and references therein) with considerable inter-study differences. A comprehensive review by Godefroid et al. (2022) documented that the number of affected biological categories in tropical scleractinians increases with decreasing pH.

Combined warming and acidification generally exhibit stronger effects than either stressor alone (Harvey et al., 2013). For corals, these stressors have been found to act synergistically (Anlauf et al., 2011; Dove et al., 2020; Anthony et al., 2008), with temperature often being the dominant factor in bleaching response, with acidification further impairing recovery and calcification. Mesocosm experiments exposing Hawaiian corals to both stressors revealed significant response variation by species and location (Schoepf et al., 2017; McLachlan et al., 2022), suggesting adaptation mechanisms may exist for some populations (Palumbi et al., 2014). A recent mesocosm study carried out over the course of two years revealed that coral reef communities can persist with altered composition under mitigated future greenhouse gas emissions (Jury et al., 2024).

For Hawaiian reefs, the interaction between warming and hypoxia could be problematic in sheltered bays and lagoons where stratification limits water mixing, potentially creating hypoxic "dead zones" during marine heatwaves (Hughes et al., 2020; Altieri et al., 2017). In contrast, macroalgae can exhibit enhanced growth under high temperature and high acidity (Gao et al., 2019), potentially accelerating phase shifts from coral to algal dominance.

The ocean around Hawai'i is also home to several phytoplankton species that may be affected by thermal stress and/or OA. Cyanobacteria, namely *Prochlorococcus* and

Synechococcus, are the primary contributor to the autotrophic biomass in the oligotrophic North Pacific. Growth rates of *Prochlorococcus* in the North Pacific were shown to increase with increasing temperatures (Ribalet et al., 2015). Based on a relationship between temperature and abundance, Flombaum et al. (2013) estimated that end-of-century warming might lead to a 20 %–30 % increase in *Prochlorococcus* and a 20 % increase in *Synechococcus* in subtropical and tropical waters. However, a recent study by Ribalet et al. (2025) reported sharply declining division rates for *Prochlorococcus* at temperatures above 28 °C and projected a substantial decline in *Prochlorococcus* production for tropical waters under moderate and high warming scenarios.

Coccolithophores also play an important role in the phytoplankton composition around Stn. ALOHA, mainly in spring and fall (Cortés et al., 2001). Numerous studies have documented reduced calcification rates for coccolithophores under OA conditions (Hutchins and Fu, 2017) (and references therein). In addition, warming has also been shown to have the potential of decreasing calcification, and this effect can even be exacerbated by OA conditions (Hutchins and Fu, 2017) (and references therein).

N_2 fixation can make up a substantial fraction of total new production around Hawai'i (Karl et al., 1997; Montoya et al., 2004). Studies suggest that nitrogen fixers may thrive under climate change. Meta-analysys of published studies concluded that diazotrophs may prosper under OA (Dutkiewicz et al., 2015; Hutchins and Fu, 2017). However, it should be noted that Gradoville et al. (2014) did not find a consistent increase of N_2 fixation for *Trichodesmium* under elevated CO_2 conditions at Stn. ALOHA. Since enzymatic processes facilitating N_2 fixation are heavily inhibited by oxygen, low O_2 conditions as projected by our study might benefit diazotrophs additionally (Sohm et al., 2011).

Copepods play an essential role in the Hawaiian (and global) foodweb by transferring energy from phytoplankton to higher trophic levels. Body size of copepods was shown to decrease with increasing temperatures across the present-day ocean (Brandão et al., 2021; Campbell et al., 2021). This suggests that warming (gradual or as frequent upper ocean heat stress) will lead to changes in the regional copepod composition and generally favor the dominance of smaller copepods (with impacts on predator-prey dynamics and higher levels of the foodweb). Conversely, the impacts of OA on copepods remain unclear. The comprehensive review by Wang et al. (2018) concluded that effects appear to strongly depend on species and life-stage. For the combined effect of high temperature and high acidity, results by Dam et al. (2021) point to reduced reproduction success and fitness but also evolutionary adaptation.

Besides copepods, the ocean around Hawai'i is also home to pteropods (Steinberg et al., 2008). Pteropods have been shown to be affected by all three stressors considered in our study (Bednaršek et al., 2016). OA poses a threat to the shell formation of (thecosome) pteropods, and shell degradation was found even for aragonite saturation states well above the thermodynamic threshold (Bednaršek et al., 2016) (and references therein). Due to the strong vertical gradients in the stressors considered here, diel vertical migration exposes pteropods (and other vertically migrating zooplankton) naturally to higher variability in temperature, acidity, and oxygen. However, only for acidity and $[O_2]$ may this exposure prepare pteropods for projected future conditions. Furthermore, it must be noted that pteropods around Stn. ALOHA are found in the upper 500 m during daytime (with highest concentrations around 125 m (Steinberg et al., 2008)). Given that the mean aragonite saturation horizon is projected to shoal to depths of about 250 m under the SSP3-7.0 scenario (Fig. 2b), it is reasonable to assume that vertical migration characteristics (and with it, predator-prey dynamics) might change substantially. Metabolic rates of pteropods increase with increasing temperature, in turn elevating their oxygen requirements. With the combination of warming temperatures and declining oxygen concentrations (and aragonite saturation state), it can be expected that processes such as growth, reproduction, and shell formation will be negatively affected (Bednaršek et al., 2016) (and references therein).

With respect to higher predators, it can be said that oxygen loss will likely be the most important of the three considered stressors. Fish responses to decreased oxygen conditions include impaired growth, reduced reproduction, decreased immune response, altered migratory behavior, and many others (Breitburg et al., 2018; Kim et al., 2023) (and references therein). Furthermore, fish aerobic capacity is reduced, with elevated CO_2 and temperature lowering metabolic scope (Munday et al., 2009). Specifically, tuna – one of the most valuable fish for Hawaiian waters – are known to aggregate in anti-cyclonic eddies due to the higher temperatures and oxygen concentrations at deeper layers (Xing et al., 2023). Given that our projections show that it will be in those circulation features where CEs will mainly be found, predation behavior of tuna might change with unclear consequences for Hawaiian fisheries. The combination of low oxygen and acidification predominantly shows additive effects on bivalve molluscs and fish, though synergistic interactions have been observed (Gobler and Baumann, 2016; Gobler et al., 2014; Miller et al., 2016). The disturbance to pH balance requires compensatory mechanisms that consume energy and further reduce performance under oxygen-limiting conditions.

The above list of potential impacts is far from exhaustive and the main shortcoming is given by the lack of studies addressing the exposure to multiple stressors – for Hawaiian waters and elsewhere. Given our modeling results and the harmful effects reported for high T and acidity as well as O_2 loss, systematic studies of the combined effects of compound events on marine organisms in Hawai'i are needed for robust projections of the future well-being of the Hawaiian ecosystem.

4 Conclusions

We have presented the first projections of future compound events for the Main Hawaiian Islands for the 21st century. Using a high-resolution physical/biogeochemical model and three different greenhouse gas emission scenarios, we have analyzed the spatial and temporal characteristics of combined events made up of extreme heat stress, acidity, and low oxygen. Our results show that regional mesoscale dynamics that are not captured by global climate models are largely responsible for shaping spatial patterns of event characteristics and differences within the domain. We have found that duration, combined intensity, and severity of compound events near the surface primarily scale with the atmospheric CO_2 concentration, while they keep increasing at deeper layers even when atmospheric CO_2 levels off or decreases. Combined compound event intensities are mostly dominated by the contribution of high acidity. The exceedance of the acidity threshold in the near-surface is projected to become a permanent feature around the year 2040 in all three SSP scenarios, while the seasonal cycle in temperature and oxygen concentrations helps to keep the duration of threshold exceedance much shorter for these variables. Our numerical model setup has also allowed us to analyze the role of tidal variability in shaping compound event characteristics. Our results show that the larger natural-variability envelope that results from accounting for tidal variability can delay the onset of compound events by decades and decrease their duration and combined intensity significantly. While this only affects a small number of near-shore locations, further studying the effect of tidal variability will be critical to robustly assess the vulnerability of coastal areas around Hawai'i and other coastal areas.

Laboratory and field studies documenting potential effects of multi-stressor events are still very limited. However, given the countless harmful effects documented for high temperature, high acidity, or low oxygen as single stressors, it is reasonable to assume that under unabated GHG emissions, the Hawaiian ecosystems will be subject to substantial changes in composition and predator-prey dynamics, forced displacement, and migration, as well as compression or loss of habitat. In view of our results and the results of others, it is now essential to gain an in-depth understanding of the effects of compound events on marine organisms and the different ecosystems as a whole. Furthermore, an extended network of biogeochemical sensors with high ($\sim$ hourly) temporal resolution covering, in particular, tidally-affected areas and depths is desirable for an observation-based determination of the natural-variability envelope that is used as a baseline for determining event thresholds for different stressors.

Appendix A: Additional Figures

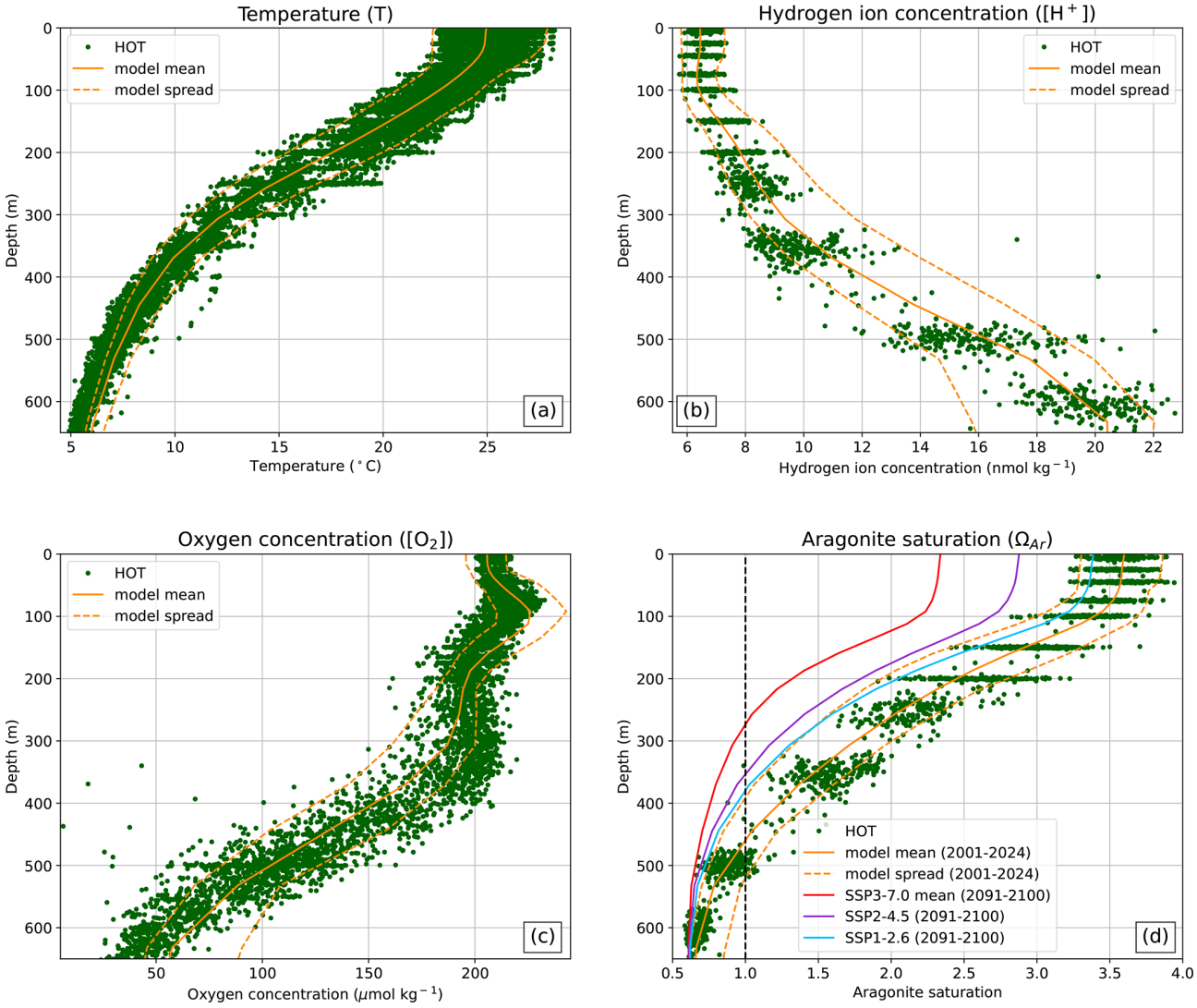


Figure A1. Comparison of simulated profiles to data gathered by the Hawai'i Ocean Time Series (HOT) program for the time period 2001–2024. **(a)**: Potential temperature (°C) measured for HOT bottle data (green dots) and simulated by the model at the Station ALOHA location (orange lines). A mean over the time period 2001–2024 and all five simulation is shown by the solid line. Dashed lines indicate temporal spread as well as spread between simulations. **(b–d)**: Same as **(a)** for variables indicated in the panels. Panel **(d)** also includes projections of the aragonite saturation (Ω_{Ar}) profile for the Station ALOHA location for the different scenarios as indicated in the panel. Dashed vertical line in panel **(d)** indicates aragonite saturation threshold of $\Omega_{Ar} = 1$.

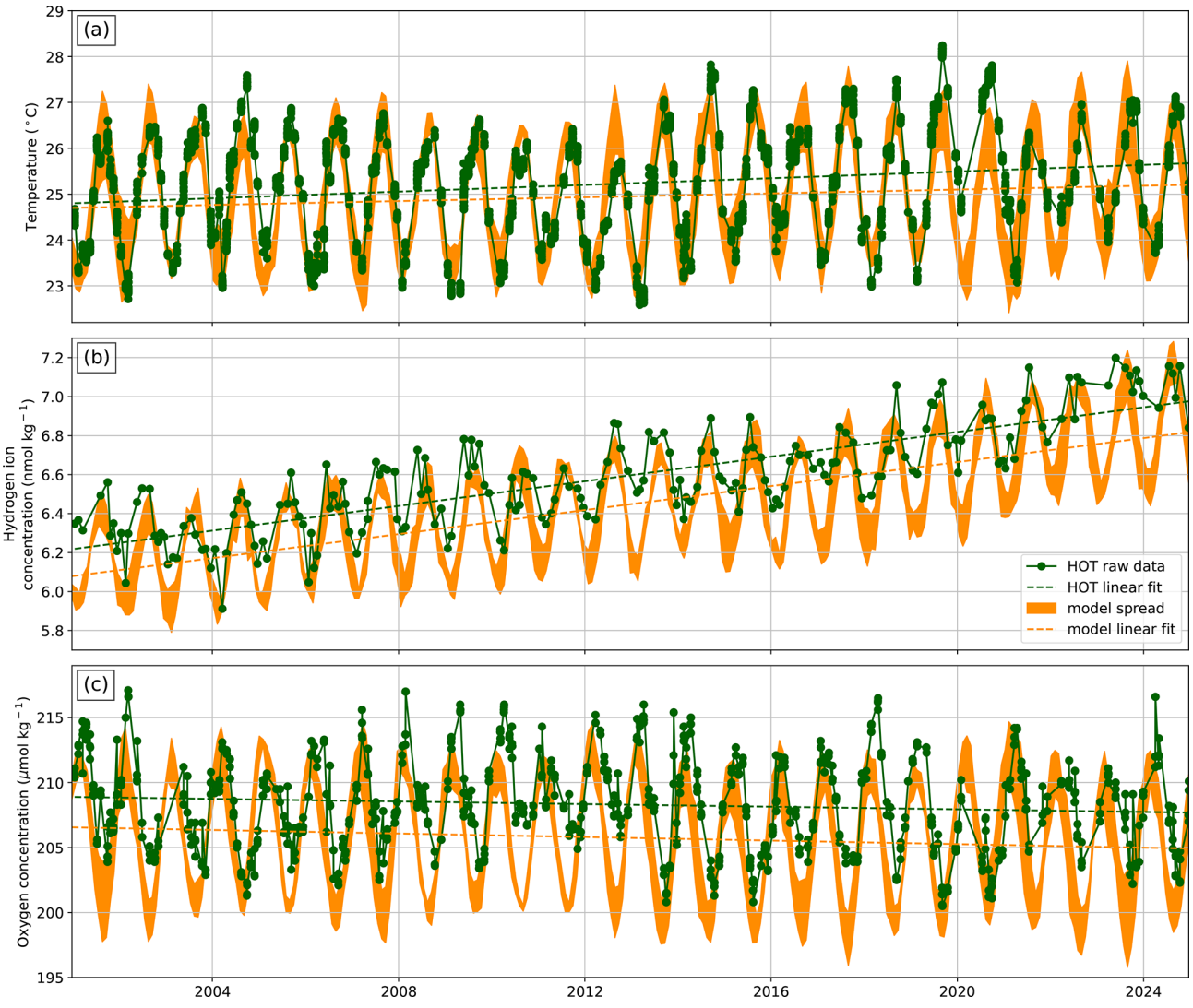


Figure A2. Comparison of simulated surface time series to data gathered by the Hawai'i Ocean Time Series (HOT) program for the time period 2001–2024. **(a)**: Potential temperature (°C) measured for HOT bottle data (green dots) and simulated by the model at the Station ALOHA location (orange swath). The range of all five simulation is shown for the model data. Dashed lines indicate linear fits of the raw data. **(b, c)**: Same as **(a)** for variables indicated in the panels.

Table A1. Modeled and observed temperature (T), hydrogen ion concentration ($[H^+]$), and oxygen concentration ($[O_2]$) for Station ALOHA location. Temporal averages and linear regression slopes calculated for the time period 2001–2024. See Sect. 2.1 and Fig. A2 for details.

parameter	T	$[H^+]$	$[O_2]$
modeled mean	24.7°	6.05 nmol kg^{-1}	206.6 µmol kg^{-1}
modeled mean range	24.3–25.1°	6.04–6.05 nmol kg^{-1}	205.4–207.9 µmol kg^{-1}
observed mean	24.8°	6.19 nmol kg^{-1}	208.9 µmol kg^{-1}
modeled mean slope	0.21 ° per decade	0.31 nmol kg^{-1} per decade	−0.68 µmol kg^{-1} per decade
modeled slope range	0.00–0.43 ° per decade	0.30–0.33 nmol kg^{-1} per decade	−0.15 to −1.38 µmol kg^{-1} per decade
observed slope	0.36 ° per decade	0.32 nmol kg^{-1} per decade	−0.50 µmol kg^{-1} per decade

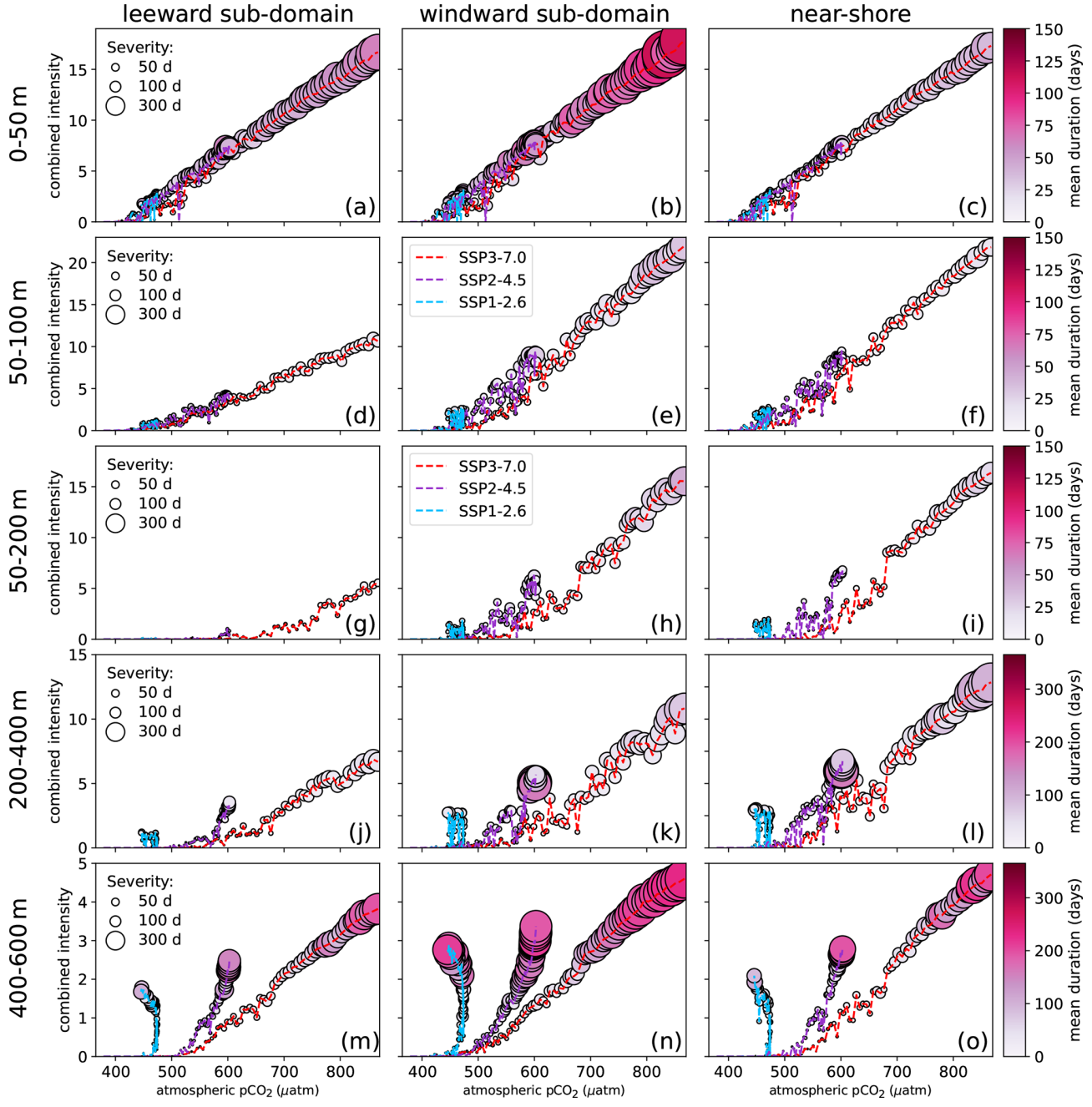


Figure A3. Projected compound event characteristics (CECs) plotted versus atmospheric pCO_2 concentration. CECs were spatially averaged for leeward, windward, and near-shore sub-domains (black lines in Fig. 1) and different depth bins as indicated on the left. Colors: annual-mean duration (days), sizes of circles: annual-mean severity (days). Greenhouse gas scenarios are indicated by line colors. Red: mean of all three SSP3-7.0 scenarios, purple: SSP2-4.5 scenario, cyan: SSP1-2.6 scenario.

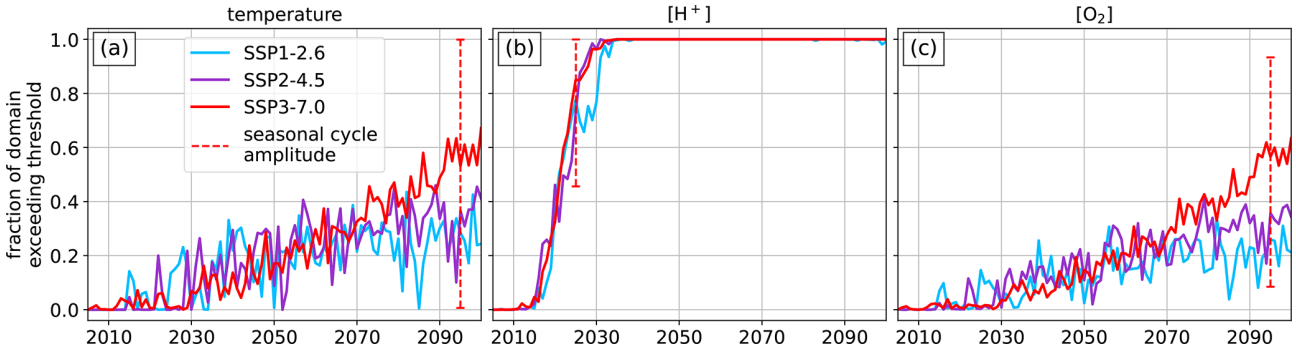


Figure A4. Fraction of domain exceeding threshold for the 0–50 m depth bin. Red: mean of all three SSP3-7.0 simulations, purple: SSP2-4.5 scenario, cyan: SSP1-2.6 scenario. Data shown are calculated based on daily-mean fractions. Annual-mean is shown for clarity. Seasonal cycle amplitude for 1 year is indicated by dashed line for a mean of all three SSP3-7.0 simulations. Threshold for hydrogen ion concentration ($[H^+]$) is permanently exceeded in the entire domain around the year 2040 in all three scenarios.

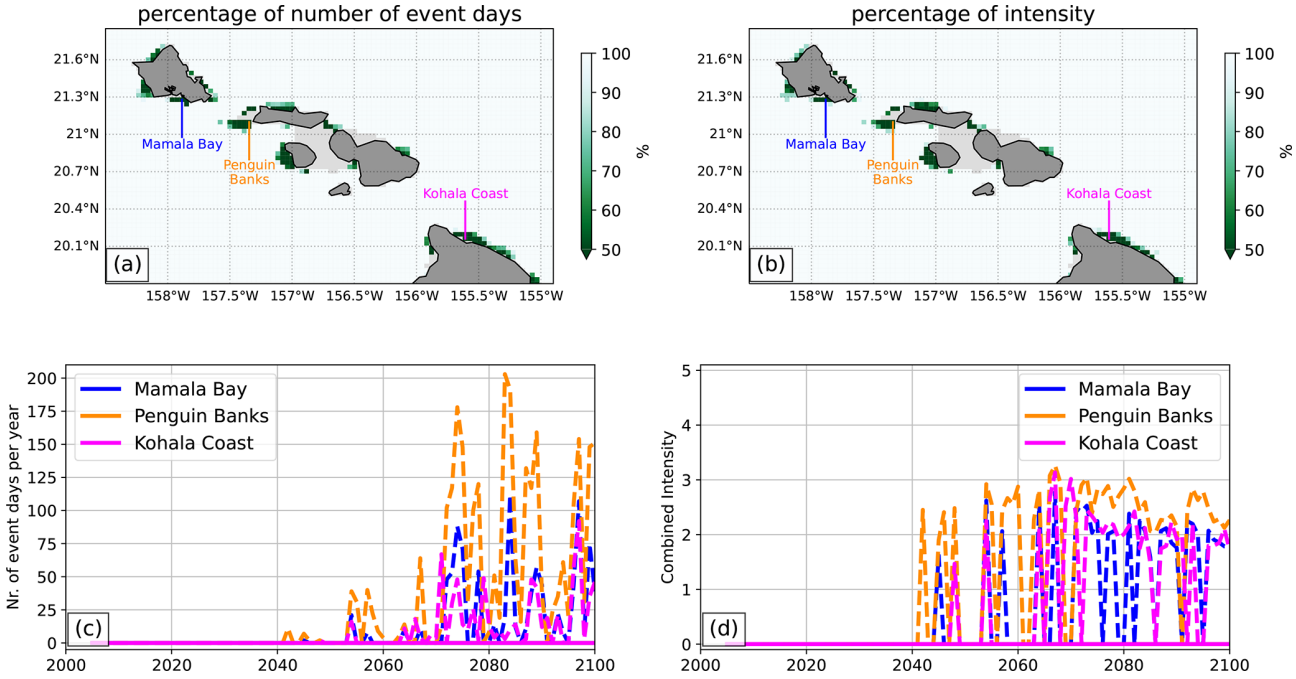


Figure A5. Effect of tides on compound event characteristics at the 100–200 m depth bin for the SSP1-2.6 scenario. Please note that only one SSP1-2.6 simulation was available impeding averaging over interannual variability. **(a)**: Percentage of number of event days (%, averaged for time period 2090–2099) derived when tidal variability is taken into account as compared to thresholds solely based on daily-mean values. **(b)**: Same as **(a)** for combined intensity. **(c)**: Timeseries of number of event days per year (days) for grid points depicted in upper panels. Dashed lines: Event thresholds based on daily-mean data. Solid lines: Event thresholds based on hourly data. **(d)**: Same as **(c)** for combined intensity. See Sect. 3.4 for details and Sect. 2.2 for calculation.

Data availability. Simulated data shown in the figures can be found at: https://osf.io/by729/ (last access: 19 October 2026).

Author contributions. TF conceived the study. TF and BSP designed and conducted the model simulations. TF and LH analyzed the model output. TF wrote the manuscript with input from all coauthors.

Competing interests. The contact author has declared that none of the authors has any competing interests.

Disclaimer. Publisher's note: Copernicus Publications remains neutral with regard to jurisdictional claims made in the text, published maps, institutional affiliations, or any other geographical representation in this paper. The authors bear the ultimate responsibility for providing appropriate place names. Views expressed in the text are those of the authors and do not necessarily reflect the views of the publisher.

Acknowledgements. We thank two anonymous reviewers along with the editor, Tyler Cyronak, for their constructive comments that helped to improve the manuscript. This is SOEST publication number 12209.

Financial support. This research has been supported by the National Oceanic and Atmospheric Administration (grant nos. NA21OAR0170191, NA20OAR4310445, NA24OARX431C0048).

Review statement. This paper was edited by Tyler Cyronak and reviewed by two anonymous referees.

References

Altieri, A. H., Harrison, S. B., Seemann, J., Collin, R., Diaz, R. J., and Knowlton, N.: Tropical dead zones and mass mortalities on coral reefs, P. Natl. Acad. Sci. USA, 114, 3660–3665, https://doi.org/10.1073/pnas.1621517114, 2017.

Amaya, D. J., Jacox, M. G., Fewings, M. R., Saba, V. S., Stuecker, M. F., Rykaczewski, R. R., Ross, A. C., Stock, C. A., Capotondi, A., Petrik, C. M., Bograd, S. J., Alexander, M. A., Cheng, W., Hermann, A. J., Kearney, K. A., and Powell, B. S.: Marine heatwaves need clear definitions so coastal communities can adapt, Nature, 616, 29–32, https://doi.org/10.1038/d41586-023-00924-2, 2023.

Anlauf, H., D'Croz, L., and O'Dea, A.: A corrosive concoction: The combined effects of ocean warming and acidification on the early growth of a stony coral are multiplicative, J. Exp. Mar. Biol. Ecol., 397, 13–20, https://doi.org/10.1016/j.jembe.2010.11.009, 2011.

Anthony, K. R. N., Kline, D. I., Diaz-Pulido, G., Dove, S., and Hoegh-Guldberg, O.: Ocean acidification causes bleaching and productivity loss in coral reef builders, P. Natl. Acad. Sci. USA, 105, 17442–17446, https://doi.org/10.1073/pnas.0804478105, 2008.

Asner, G. P., Vaughn, N. R., Martin, R. E., Foo, S. A., Heckler, J., Neilson, B. J., and Gove, J. M.: Mapped coral mortality and refugia in an archipelago-scale marine heat wave, P. Natl. Acad. Sci. USA, 119, e2123331119, https://doi.org/10.1073/pnas.2123331119, 2022.

Azevedo Correia de Souza, J. M. and Powell, B.: Different approaches to model the nearshore circulation in the south shore of O'ahu, Hawaii, Ocean Sci., 13, 31–46, https://doi.org/10.5194/os-13-31-2017, 2017.

Azevedo Correia de Souza,, J. M., Powell, B. S., Castillo-Trujillo, A. C., and Flament, P.: The Vorticity Balance of the Ocean Surface in Hawaii from a Regional Reanalysis, J. Phys. Oceanogr., 45, 424–440, https://doi.org/10.1175/JPO-D-14-0074.1, 2015.

Bahr, K. D., Jokiel, P. L., and Rodgers, K. S.: The 2014 coral bleaching and freshwater flood events in Kāne'ohe Bay, Hawai'i, PeerJ, 3, e1136, https://doi.org/10.7717/peerj.1136, 2015.

Barone, B., Coenen, A. R., Beckett, S. J., McGillicuddy Jr, D. J., Weitz, J. S., and Karl, D. M.: The ecological and biogeochemical state of the North Pacific Subtropical Gyre is linked to sea surface height, J. Mar. Res., 77, 215–245, 2019.

Barone, B., Church, M. J., Dugenne, M., Hawco, N. J., Jahn, O., White, A. E., John, S. G., Follows, M. J., DeLong, E. F., and Karl, D. M.: Biogeochemical dynamics in adjacent mesoscale eddies of opposite polarity, Global Biogeochem. Cy., 36, e2021GB007115, https://doi.org/10.1029/2021GB007115, 2022.

Bednaršek, N., Harvey, C. J., Kaplan, I. C., Feely, R. A., and Možina, J.: Pteropods on the edge: Cumulative effects of ocean acidification, warming, and deoxygenation, Prog. Oceanogr., 145, 1–24, https://doi.org/10.1016/j.pocean.2016.04.002, 2016.

Behrens, M. K., Pahnke, K., Schnetger, B., and Brumsack, H.-J.: Sources and processes affecting the distribution of dissolved Nd isotopes and concentrations in the West Pacific, Geochim. Cosmochim. Ac., 222, 508–534, https://doi.org/10.1016/j.gca.2017.11.008, 2018.

Bostock, H. C., Opdyke, B. N., and Williams, M. J.: Characterising the intermediate depth waters of the Pacific Ocean using δ^{13}C and other geochemical tracers, Deep-Sea Res. Pt. I, 57, 847–859, https://doi.org/10.1016/j.dsr.2010.04.005, 2010.

Brandão, M. C., Benedetti, F., Martini, S., Soviadan, Y. D., Irisson, J.-O., Romagnan, J.-B., Elineau, A., Desnos, C., Jalabert, L., Freire, A. S., Picheral, M., Guidi, L., Gorsky, G., Bowler, C., Karp-Boss, L., Henry, N., de Vargas, C., Sullivan, M. B., Coordinators, T. O. C., Stemmann, L., and Lombard, F.: Macroscale patterns of oceanic zooplankton composition and size structure, Sci. Rep., 11, 15714, https://doi.org/10.1038/s41598-021-94615-5, 2021.

Breitburg, D., Levin, L. A., Oschlies, A., Grégoire, M., Chavez, F. P., Conley, D. J., Garçon, V., Gilbert, D., Gutiérrez, D., Isensee, K., Jacinto, G. S., Limburg, K. E., Montes, I., Naqvi, S. W. A., Pitcher, G. C., Rabalais, N. N., Roman, M. R., Rose, K. A., Seibel, B. A., Telszewski, M., Yasuhara, M., and Zhang, J.: Declining oxygen in the global ocean and coastal waters, Science, 359, https://doi.org/10.1126/science.aam7240, 2018.

Burger, F. A., Terhaar, J., and Frölicher, T. L.: Compound marine heatwaves and ocean acidity extremes, Nat. Commun., 13, 4722, https://doi.org/10.1038/s41467-022-32120-7, 2022.

Calil, P. H. R., Richards, K. J., Jia, Y., and Bidigare, R. R.: Eddy activity in the lee of the Hawaiian Islands, Deep-Sea Res. Pt. II, 55, 1179–1194, https://doi.org/10.1016/j.dsr2.2008.01.008, 2008.

Campbell, M. D., Schoeman, D. S., Venables, W., Abu-Alhaija, R., Batten, S. D., Chiba, S., Coman, F., Davies, C. H., Edwards, M., Eriksen, R. S., Everett, J. D., Fukai, Y., Fukuchi, M., Esquivel Garrote, O., Hosie, G., Huggett, J. A., G, J. D., Kitchener, J. A., Koubbi, P., McEnnulty, F. R., Muxagata, E., Ostle, C., Robinson, K. V., Slotwinski, A., Swadling, K. M., Takahashi, K. T., Tonks, M., Uribe-Palomino, J., Verheye, H. M., Wilson, W. H., M, W. M., Yamaguchi, A., Zhang, W., and Rishardson, A. J.: Testing Bergmann's rule in marine copepods, Ecography, 44, 1283–1295, https://doi.org/10.1111/ecog.05545, 2021.

Chan, N. C. and Connolly, S. R.: Sensitivity of coral calcification to ocean acidification: a meta-analysis, Glob. Change Biol., 19, 282–290, https://doi.org/10.1111/gcb.12011, 2013.

Chavanne, C., Flament, P., Lumpkin, R., Dousset, B., and Bentamy, A.: Scatterometer observations of wind variations induced by oceanic islands: Implications for wind-driven ocean circulation, Can. J. Remote Sens., 28, 466–474, https://doi.org/10.5589/m02-047, 2002.

Chelton, D. B. and Schlax, M. G.: Global observations of oceanic Rossby waves, Science, 272, 234–238, https://doi.org/10.1126/science.272.5259.234, 1996.

Cortés, M. Y., Bollmann, J., and Thierstein, H. R.: Coccolithophore ecology at the HOT station ALOHA, Hawaii, Deep-Sea Res. Pt. II, 48, 1957–1981, https://doi.org/10.1016/S0967-0645(00)00165-X, 2001.

Cross, J., Macdonald, A., Alin, S., Wanninkhof, R., Dickson, A., Carlson, C., Johnson, G., Baringer, M., Mordy, C., Langdon, C., Key, R., McNichol, A., Bullister, J., Jenkins, W., and Nelson, N.: Carbon Dioxide, Hydrographic, and Chemical Data Obtained During the R/V Ron Brown Repeat Hydrography Cruises in the Pacific Ocean: GO-SHIP Section P16N_2015, Legs 1 and 2 (10 April–27 June, 2015), Tech. rep., Carbon Dioxide Information Analysis Center, Oak Ridge National Laboratory, US Department of Energy, Oak Ridge, TN, https://doi.org/10.3334/cdiac/otg.go_ship_p16n_2015, 2015.

Dam, H. G., Demayo, J. A., Park, G., Norton, L., He, X., Finiguerra, M. B., Baumann, H., Brennan, R. S., and Pespeni, M. H.: Rapid, but limited, zooplankton adaptation to simultaneous warming and acidification, Nat. Clim. Change, 11, 780–786, https://doi.org/10.1038/s41558-021-01131-5, 2021.

Danabasoglu, G., Lamarque, J.-F., Bacmeister, J., Bailey, D. A., DuVivier, A. K., Edwards, J., Emmons, L. K., Fasullo, J., Garcia, R., Gettelman, A., Hannay, C., Holland, M. M., Large, W. G., Lauritzen, P. H., Lawrence, D. M., Lenaerts, J. T. M., Lindsay, K., Lipscomp, W. H., Mills, M. J., Neale, R., Oleson, K. W., Otto-Bliesner, B., Phillips, A. S., Sacks, W., Tilmes, S., van Kampenhout, L., Vertenstein, M., Bertini, A., Dennis, J., Deser, C., Fisher, C., Fox-Kemper, B., Kay, J. E., Kinnison, D., Kushner, P. J., Larson, V. E., Long, M. C., Mickelson, S., Moore, J. K., Nienhouse, E., Polvani, L., Rasch, P. J., and Strand, W. G.: The community earth system model version 2 (CESM2), J. Adv. Model. Earth Sy., 12, e2019MS001916, https://doi.org/10.1029/2019MS001916, 2020.

Dove, S. G., Brown, K. T., Van Den Heuvel, A., Chai, A., and Hoegh-Guldberg, O.: Ocean warming and acidification uncouple calcification from calcifier biomass which accelerates coral reef decline, Communications Earth Environment, 1, 1–9, https://doi.org/10.1038/s43247-020-00054-x, 2020.

Dutkiewicz, S., Morris, J. J., Follows, M. J., Scott, J., Levitan, O., Dyhrman, S. T., and Berman-Frank, I.: Impact of ocean acidification on the structure of future phytoplankton communities, Nat. Clim. Change, 5, 1002–1006, https://doi.org/10.1038/nclimate2722, 2015.

Feloy, K., Powell, B. S., and Friedrich, T.: Remote impacts of cyclonic eddies on productivity around the Main Hawaiian Islands, Journal of Geophysical Research: Oceans, 129, e2023JC020670, https://doi.org/10.1029/2023JC020670, 2024.

Flombaum, P., Gallegos, J. L., Gordillo, R. A., Rincón, J., Zabala, L. L., Jiao, N., Karl, D. M., Li, W. K., Lomas, M. W., Veneziano, D., Vera, C. S., Vrugt, J. A., and Martiny, A. C.: Present and future global distributions of the marine Cyanobacteria *Prochlorococcus* and *Synechococcus*, P. Natl. Acad. Sci. USA, 110, 9824–9829, https://doi.org/10.1073/pnas.1307701110, 2013.

Friedrich, T., Powell, B., Stock, C., Hahn-Woernle, L., Dussin, R., and Curchitser, E.: Drivers of phytoplankton blooms in Hawaii: A regional model study, Journal of Geophysical Research: Oceans, 126, e2020JC017069, https://doi.org/10.1029/2020JC017069, 2021.

Friedrich, T., Powell, B., Gunnarson, J., Liu, G., Giardina, S., Stuecker, M., Hošeková, L., Feloy, K., and Stock, C.: Submesoscale-permitting physical/biogeochemical future projections for the main Hawaiian Islands, J. Adv. Model. Earth Sy., 16, e2023MS003855, https://doi.org/10.1029/2023MS003855, 2024.

Gao, K., Beardall, J., Häder, D.-P., Hall-Spencer, J. M., Gao, G., and Hutchins, D. A.: Effects of Ocean Acidification on Marine Photosynthetic Organisms Under the Concurrent Influences of Warming, UV Radiation, and Deoxygenation, Frontiers in Marine Science, 6, 463462, https://doi.org/10.3389/fmars.2019.00322, 2019.

Gobler, C. J. and Baumann, H.: Hypoxia and acidification in ocean ecosystems: coupled dynamics and effects on marine life, Biol. Lett.-UK, 12, 20150976., https://doi.org/10.1098/rsbl.2015.0976, 2016.

Gobler, C. J., DePasquale, E. L., Griffith, A. W., and Baumann, H.: Hypoxia and Acidification Have Additive and Synergistic Negative Effects on the Growth, Survival, and Metamorphosis of Early Life Stage Bivalves, PLOS ONE, 9, e83648, https://doi.org/10.1371/journal.pone.0083648, 2014.

Godefroid, M., Dupont, S., Metian, M., and Hédouin, L.: Two decades of seawater acidification experiments on tropical scleractinian corals: Overview, meta-analysis and perspectives, Mar. Pollut. Bull., 178, 113552, https://doi.org/10.1016/j.marpolbul.2022.113552, 2022.

Gradoville, M. R., White, A. E., Böttjer, D., Church, M. J., and Letelier, R. M.: Diversity trumps acidification: Lack of evidence for carbon dioxide enhancement of *Trichodesmium* community nitrogen or carbon fixation at Station ALOHA, Limnol. Oceanogr., 59, 645–659, https://doi.org/10.4319/lo.2014.59.3.0645, 2014.

Gruber, N., Boyd, P. W., Frölicher, T. L., and Vogt, M.: Biogeochemical extremes and compound events in the ocean, Na-

ture, 600, 395–407, https://doi.org/10.1038/s41586-021-03981-7, 2021.

Harvey, B. P., Gwynn-Jones, D., and Moore, P. J.: Meta-analysis reveals complex marine biological responses to the interactive effects of ocean acidification and warming, Ecol. Evol., 3, 1016–1030, https://doi.org/10.1002/ece3.516, 2013.

Hauri, C., Friedrich, T., and Timmermann, A.: Abrupt onset and prolongation of aragonite undersaturation events in the Southern Ocean, Nat. Clim. Change, 6, 172–176, https://doi.org/10.1038/nclimate2844, 2016.

Hauri, C., Pages, R., Hedstrom, K., Doney, S. C., Dupont, S., Ferriss, B., and Stuecker, M. F.: More than marine heatwaves: A new regime of heat, acidity, and low oxygen compound extreme events in the Gulf of Alaska, AGU Advances, 5, e2023AV001039, https://doi.org/10.1029/2023AV001039, 2024.

Hošeková, L., Friedrich, T., Powell, B. S., and Sabine, C. L.: Patterns of ocean acidification emergence in the Hawaiian Islands using dynamically downscaled projections, J. Geophys. Res.-Oceans, 130, e2024JC021903, https://doi.org/10.1029/2024JC021903, 2025.

Hughes, D. J., Alderdice, R., Cooney, C., Kühl, M., Pernice, M., Voolstra, C. R., and Suggett, D. J.: Coral reef survival under accelerating ocean deoxygenation, Nat. Clim. Change, 10, 296–307, https://doi.org/10.1038/s41558-020-0737-9, 2020.

Humphreys, M. P., Lewis, E. R., Sharp, J. D., and Pierrot, D.: PyCO2SYS v1.8: marine carbonate system calculations in Python, Geosci. Model Dev., 15, 15–43, https://doi.org/10.5194/gmd-15-15-2022, 2022.

Hutchins, D. A. and Fu, F.: Microorganisms and ocean global change, Nat. Microbiol., 2, 1–11, https://doi.org/10.1038/nmicrobiol.2017.58, 2017.

IPCC: Synthesis report of the IPCC Sixth Assessment Report (AR6), Longer report, IPCC, https://doi.org/10.59327/ipcc/ar6-9789291691647, 2023.

Jia, Y., Calil, P. H. R., Chassignet, E., Metzger, E., Potemra, J., Richards, K., and Wallcraft, A. J.: Generation of mesoscale eddies in the lee of the Hawaiian Islands, J. Geophys. Res.-Oceans, 116, https://doi.org/10.1029/2011JC007305, 2011.

Jokiel, P. L. and Brown, E. K.: Global warming, regional trends and inshore environmental conditions influence coral bleaching in Hawaii, Glob. Change Biol., 10, 1627–1641, https://doi.org/10.1111/j.1365-2486.2004.00836.x, 2004.

Jury, C. P., Bahr, K. D., Cros, A., Dobson, K. L., Freel, E. B., Graham, A. T., McLachlan, R. H., Nelson, C. E., Price, J. T., Rocha de Souza, M., Shizuru, L., Smith, C. M., Sparagon, W. J., Squair, C. A., Timmers, M. A., Vincente, J., Webb, M. K., Yamase, N. H., Grotolli, A. G., and Toonen, R. J.: Experimental coral reef communities transform yet persist under mitigated future ocean warming and acidification, P. Natl. Acad. Sci. USA, 121, e2407112121, https://doi.org/10.1073/pnas.2407112121, 2024.

Karl, D. M. and Church, M. J.: Station ALOHA: a gathering place for discovery, education, and scientific collaboration, Limnol. Oceanogr. Bulletin, 28, 10–12, https://doi.org/10.1002/lob.10285, 2018.

Karl, D. M., Letelier, R., Tupas, L., Dore, J., Christian, J., and Hebel, D.: The role of nitrogen fixation in biogeochemical cycling in the subtropical North Pacific Ocean, Nature, 388, 533–538, https://doi.org/10.1038/41474, 1997.

Kim, H., Franco, A. C., and Sumaila, U. R.: A selected review of impacts of ocean deoxygenation on fish and fisheries, Fishes, 8, 316, https://doi.org/10.3390/fishes8060316, 2023.

Kwiatkowski, L., Torres, O., Bopp, L., Aumont, O., Chamberlain, M., Christian, J. R., Dunne, J. P., Gehlen, M., Ilyina, T., John, J. G., Lenton, A., Li, H., Lovenduski, N. S., Orr, J. C., Palmieri, J., Santana-Falcón, Y., Schwinger, J., Séférian, R., Stock, C. A., Tagliabue, A., Takano, Y., Tjiputra, J., Toyama, K., Tsujino, H., Watanabe, M., Yamamoto, A., Yool, A., and Ziehn, T.: Twenty-first century ocean warming, acidification, deoxygenation, and upper-ocean nutrient and primary production decline from CMIP6 model projections, Biogeosciences, 17, 3439–3470, https://doi.org/10.5194/bg-17-3439-2020, 2020.

Matthews, D., Powell, B., and Milliff, R.: Dominant spatial variability scales from observations around the Hawaiian Islands, Deep-Sea Res. Pt. I, 58, 979–987, https://doi.org/10.1016/j.dsr.2011.07.004, 2011.

Matthews, D., Powell, B. S., and Janeković, I.: Analysis of four-dimensional variational state estimation of the Hawaiian waters, J. Geophys. Res.-Oceans, 117, C03013, https://doi.org/10.1029/2011JC007575, 2012.

McClanahan, T.: Coral responses to climate change exposure, Environ. Res. Lett., 17, 073001, https://doi.org/10.1088/1748-9326/ac7478, 2022.

McLachlan, R. H., Price, J. T., Muñoz-Garcia, A., Weisleder, N. L., Levas, S. J., Jury, C. P., Toonen, R. J., and Grottoli, A. G.: Physiological acclimatization in Hawaiian corals following a 22-month shift in baseline seawater temperature and pH, Sci. Rep., 12, 1–11, https://doi.org/10.1038/s41598-022-06896-z, 2022.

Merrifield, M. A. and Holloway, P. E.: Model estimates of M_2 internal tide energetics at the Hawaiian Ridge, J. Geophys. Res.-Oceans, 107, 5–1, https://doi.org/10.1029/2001JC000996, 2002.

Miller, S. H., Breitburg, D. L., Burrell, R. B., and Keppel, A. G.: Acidification increases sensitivity to hypoxia in important forage fishes, Mar. Ecol. Prog. Ser., 549, 1–8, https://doi.org/10.3354/meps11695, 2016.

Mogen, S. C., Lovenduski, N. S., Yeager, S. G., Capotondi, A., Jacox, M. G., Bograd, S., Di Lorenzo, E., Hazen, E. L., Pozo Buil, M., Kim, W., and Rosenbloom, N.: Multi-month forecasts of marine heatwaves and ocean acidification extremes, Nat. Geosci., 17, 1261–1267, https://doi.org/10.1038/s41561-024-01593-0, 2024.

Montoya, J. P., Holl, C. M., Zehr, J. P., Hansen, A., Villareal, T. A., and Capone, D. G.: High rates of N_2 fixation by unicellular diazotrophs in the oligotrophic Pacific Ocean, Nature, 430, 1027–1031, https://doi.org/10.1038/nature02824, 2004.

Munday, P. L., Crawley, N. E., and Nilsson, G. E.: Interacting effects of elevated temperature and ocean acidification on the aerobic performance of coral reef fishes, Mar. Ecol. Prog. Ser., 388, 235–242, https://doi.org/10.3354/meps08137, 2009.

Palumbi, S. R., Barshis, D. J., Traylor-Knowles, N., and Bay, R. A.: Mechanisms of reef coral resistance to future climate change, Science, 344, 895–898, https://doi.org/10.1126/science.1251336, 2014.

Partridge, D., Friedrich, T., and Powell, B. S.: Reanalysis of the PacIOOS Hawaiian Island Ocean Forecast System, an implementation of the Regional Ocean Modeling System v3.6, Geosci. Model Dev., 12, 195–213, https://doi.org/10.5194/gmd-12-195-2019, 2019.

Rainville, L., Johnston, T. S., Carter, G. S., Merrifield, M. A., Pinkel, R., Worcester, P. F., and Dushaw, B. D.: Interference pattern and propagation of the M_2 internal tide south of the Hawaiian Ridge, J. Phys. Oceanogr., 40, 311–325, https://doi.org/10.1175/2009JPO4256.1, 2010.

Ribalet, F., Swalwell, J., Clayton, S., Jiménez, V., Sudek, S., Lin, Y., Johnson, Z. I., Worden, A. Z., and Armbrust, E. V.: Light-driven synchrony of *Prochlorococcus* growth and mortality in the subtropical Pacific gyre, P. Natl. Acad. Sci. USA, 112, 8008–8012, https://doi.org/10.1073/pnas.1424279112, 2015.

Ribalet, F., Dutkiewicz, S., Monier, E., and Armbrust, E. V.: Future ocean warming may cause large reductions in *Prochlorococcus* biomass and productivity, Nat. Microbiol., 10, 2441–2453, https://doi.org/10.1038/s41564-025-02106-4, 2025.

Rodgers, K. B., Lee, S.-S., Rosenbloom, N., Timmermann, A., Danabasoglu, G., Deser, C., Edwards, J., Kim, J.-E., Simpson, I. R., Stein, K., Stuecker, M. F., Yamaguchi, R., Bódai, T., Chung, E.-S., Huang, L., Kim, W. M., Lamarque, J.-F., Lombardozzi, D. L., Wieder, W. R., and Yeager, S. G.: Ubiquity of human-induced changes in climate variability, Earth Syst. Dynam., 12, 1393–1411, https://doi.org/10.5194/esd-12-1393-2021, 2021.

Rodrigues, R., Neto, A. G., Frölicher, T., Keenlyside, N., Hobday, A., Burger, F., Bernardo, P., and Araujo, J.: Extreme Compound Events in the Equatorial and South Atlantic, Nat. Commun., 16, 3183, https://doi.org/10.1038/s41467-025-58238-y, 2025.

Schoepf, V., Jury, C. P., Toonen, R. J., and McCulloch, M. T.: Coral calcification mechanisms facilitate adaptive responses to ocean acidification, P. Roy. Soc. B-Biol. Sci., 284, https://doi.org/10.1098/rspb.2017.2117, 2017.

Shchepetkin, A. F. and McWilliams, J. C.: Quasi-Monotone Advection Schemes Based on Explicit Locally Adaptive Dissipation, Mon. Weather Rev., 126, 1541–1580, https://doi.org/10.1175/1520-0493(1998)126<1541:QMASBO>2.0.CO;2, 1998.

Shchepetkin, A. F. and McWilliams, J. C.: A method for computing horizontal pressure-gradient force in an oceanic model with a nonaligned vertical coordinate, J. Geophys. Res.-Oceans, 108, https://doi.org/10.1029/2001JC001047, 3090, 2003.

Shchepetkin, A. F. and McWilliams, J. C.: The Regional Oceanic Modeling System (ROMS): A Split-explicit, Free-surface, Topography-following-coordinate Oceanic Model, Ocean Model., 9, 347–404, https://doi.org/10.1016/j.ocemod.2004.08.002, 2005.

Sohm, J. A., Webb, E. A., and Capone, D. G.: Emerging patterns of marine nitrogen fixation, Nat. Rev. Microbiol., 9, 499–508, https://doi.org/10.1038/nrmicro2594, 2011.

Steinberg, D. K., Cope, J. S., Wilson, S. E., and Kobari, T.: A comparison of mesopelagic mesozooplankton community structure in the subtropical and subarctic North Pacific Ocean, Deep-Sea Res. Pt. II, 55, 1615–1635, https://doi.org/10.1016/j.dsr2.2008.04.025, 2008.

Stock, C. A., Dunne, J. P., and John, J. G.: Global-scale carbon and energy flows through the marine planktonic food web: An analysis with a coupled physical–biological model, Prog. Oceanogr., 120, 1–28, https://doi.org/10.1016/j.pocean.2013.07.001, 2014.

Wang, M., Jeong, C.-B., Lee, Y. H., and Lee, J.-S.: Effects of ocean acidification on copepods, Aquat. Toxicol., 196, 17–24, https://doi.org/10.1016/j.aquatox.2018.01.004, 2018.

Wong, J., Münnich, M., and Gruber, N.: Column-compound extremes in the global ocean, AGU Advances, 5, e2023AV001059, https://doi.org/10.1029/2023AV001059, 2024.

Xie, S.-P., Liu, W. T., Liu, Q., and Nonaka, M.: Far-reaching effects of the Hawaiian Islands on the Pacific ocean-atmosphere system, Science, 292, 2057–2060, https://doi.org/10.1126/science.1059781, 2001.

Xing, Q., Yu, H., Wang, H., Ito, S.-i., and Chai, F.: Mesoscale eddies modulate the dynamics of human fishing activities in the global midlatitude ocean, Fish Fish., 24, 527–543, https://doi.org/10.1111/faf.12742, 2023.

Yoshida, S., Qiu, B., and Hacker, P.: Wind-generated eddy characteristics in the lee of the island of Hawaii, J. Geophys. Res.-Oceans, 115, https://doi.org/10.1029/2009JC005417, 2010.